

Extraction of Large-Scale Coherent Structures from Large Eddy Simulation of Supersonic Jets for Shock-Associated Noise Prediction

Weiqi Shen,^{*} Trushant Patel,[†] and Steven A. E. Miller[‡]
University of Florida, Gainesville, FL, 32611, USA

Supersonic jet noise reduction has become one of the major challenges for the design of high performance aircraft. The broadband shock-associated noise (BBSAN) is analyzed using the simulation data of a heated under-expanded supersonic jet from a high-order compressible large eddy simulation solver. The flow-field results are compared with a Reynolds-averaged Navier-Stokes simulation at the same jet condition. The far-field acoustic results are validated with experimental measurements. An acoustic analogy based on the decomposition of the Navier-Stokes equations is used to analyze the noise source of BBSAN. The source term of the BBSAN is identified, which is the product of anisotropic velocities and mean pressure gradients. The source term is validated by comparing the BBSAN spectra with the measured total spectra. The BBSAN spectra in the far-field are preserved when the flow-field is reconstructed using different numbers of proper orthogonal decomposition modes at different observation angles. The majority of source intensity is distributed on the oblique shock waves and the region near the end of the potential core. Source statistics show large positive correlations paired with negative correlations at the local and neighboring shock waves.

Nomenclature

Symbols	Description	Δ	cutoff length-scale
C_w	WALE constant	γ	ratio of specific heats
c	speed of sound	μ	dynamic viscosity
D	nozzle exit diameter	μ_t	eddy viscosity
e	specific internal energy		
e_0	specific total energy	Non-Dimensional Numbers	
f	frequency	Pr	Prandtl number
\mathcal{H}	Heaviside function	Pr_t	turbulent Prandtl number
\mathbf{n}	unit normal vector	St	Strouhal number
\mathcal{P}	polynomial order		
\mathbf{q}	solution variables	Superscripts	
R	nozzle exit radius	C	corrected value
S_{ij}	strain rate tensor	I	common interface value
sgn	sign function	L	value on the left side of the interface
T_{ij}	Lighthill stress tensor	R	value on the right side of the interface
V	element volume	sgs	sub-grid scale term
$\bar{\square}$	Favre averaging	$*$	complex conjugate
$\overline{\square}$	averaging	T	transpose
\square'	derivative with respect to source time	Subscripts	
Greek Symbols		inv	inviscid component
δ	Dirac delta function	$visc$	viscous component
δ_{ij}	Kronecker delta function		

I. Introduction

NOISE radiating from supersonic jet aircraft has become a major health concern for military personnel working on the flight deck of aircraft carriers. Military personnel are constantly exposed to noises louder than 140 dB. The extreme

^{*}Ph.D. Candidate, Department of Mechanical and Aerospace Engineering, University of Florida, weiqishen1994@ufl.edu, AIAA Student Member

[†]Ph.D. Candidate, Department of Mechanical and Aerospace Engineering, University of Florida, trushant@ufl.edu, AIAA Student Member

[‡]Assistant Professor, Department of Mechanical and Aerospace Engineering, University of Florida, saem@ufl.edu, AIAA Lifetime / Senior Member

environment leads to many service-related disabilities such as tinnitus and hearing loss, which cost the US government 1.4 billion dollars every year [1]. In the future, development of supersonic commercial airliners will introduce more challenges for supersonic jet noise reduction at civilian airports.

To reduce the jet noise, it is important to understand the noise generation mechanism. Early works on jet noise [2], due to the lack of knowledge of turbulence, have considered random turbulent fluctuations as the noise source. However, after the large-scale coherent structures were identified in free shear layers [3–5], researchers now believe that both the fine-scale and the large-scale structures are responsible for the noise generation in a turbulent jet flow.

Tam [6], in his review paper, pointed out that the large-scale structures in turbulence are the dominant noise source in supersonic jets. In addition, military engines usually operate at an off-design condition during take-off, creating shock-cell structures within the jet plume. The interaction between the large-scale coherent structures in the shear layer and the shock waves leads to the generation of broadband shock-associated noise (BBSAN). The BBSAN dominates in the far-field at large angles with respect to the jet axis at mid to high frequencies.

A. Previous Approaches

Many attempts have been made to understand the noise generation mechanism of large-scale coherent structures in turbulent shear layers and jets. Tam and Chen [7] proposed a statistical model that describes large-scale turbulent structures as a linear superposition of instability waves initiated by random excitation near the nozzle lip. A year later, Tam and Morris [8] predicted acoustic radiation of sound by instability waves from plane turbulent shear layers using hydrodynamic stability theory. This method was then extended to supersonic flow by Tam and Burton [9, 10]. Alternatively, a wave packet ansatz [11] can be used to model the noise source from large-scale turbulent structures using the sound field or a velocity field measurement.

The pioneering work on BBSAN was carried out by Harper-Bourne and Fisher [12], who modeled BBSAN as discrete shock-vortex interactions. The noise was modeled for convergent nozzles using an array of point sources distributed along the shock locations at the lip-line of the jet. These point sources are correlated, creating strong noise radiation through constructive interference at observers in the far-field.

Tam and Tanna [13] proposed that BBSAN is generated by the weak interaction between downstream propagating large-scale turbulent structures and the shock cell structure of the jet. A noise intensity scaling formula and a peak frequency formula were derived using this framework. Tam [14] integrated his stochastic model for instability waves with the shock-cell structures to predict the BBSAN spectra. In this models, the jet flow is viewed as a superposition of the waveguide modes with different wavelengths of the shock-cell structure with the instability waves. Because of this superposition, the instability waves are scattered into different upstream directions. The upstream propagating waves that have supersonic phase speed generate noise through Mach wave radiation. Each waveguide mode has a different wavelength that generates a distinct noise spectrum with a spectral peak frequency. Therefore, the total shock noise spectrum is made up of the superposition of these spectra. This method successfully predicts the multiple broadband peaks in the noise spectrum and shows good agreement between the calculated and the measured spectra. Morris and Miller [15] developed an acoustic analogy to predict BBSAN based on linearized Euler equations using solutions of Reynolds-averaged Navier-Stokes (RANS) equations. In their model, the use of RANS solutions enables the prediction of the BBSAN at a wide range of operating conditions as only nozzle geometry and operating conditions are required for the prediction. Alternatively, a wave-packet like model was proposed by Suzuki [16] to predict BBSAN from large eddy simulation (LES) data.

In the past few decades, with the advancement of numerical algorithms and high performance computers, numerical methods have been applied to jet noise studies. Direct numerical simulation (DNS), which resolves the turbulent flow-field down to the smallest scale (Kolmogorov scale), requires a large number of grid points (scales with $Re^{9/4}$ where Re is the Reynolds number), making it prohibitively expensive for the simulation of high Reynolds number flows. Nevertheless, LES only resolves the most energetic scales in the turbulent flow, while modeling the smaller and less energetic scales. The required number of nodes, as estimated by Choi and Moin [17], is only of the order of $Re^{13/7}$ for wall resolved LES and Re for wall modeled LES, making it an accurate and affordable choice for jet simulations. Therefore, LES coupled with a Ffowcs-Williams and Hawkings [18] (FWH) acoustic solver to compute the far-field noise has become a popular method for the jet noise simulations.

Boersma and Lele [19] carried out LES for a low Reynolds number subsonic jet using a high-order finite difference scheme on a structured curvilinear grid. The results were compared to the direct numerical simulation (DNS) at the same condition and the LES results showed good agreement. Later, a jet with higher Reynolds number [20] was simulated using the same method. Shur et al. [21] used a structured multiblock solver to predict the noise from jets of airliner

engines. He coupled the RANS solution inside of the nozzle with the boundary condition of LES to simulate the jet flow in the freestream. With the development of unstructured solvers [22–24], nozzle geometries can be easily modeled and included in the computational domain to improve the accuracy of the simulation. Advanced techniques such as wall modelling, adaptive mesh refinement, and synthetic turbulence [25–27] were used at the nozzle inner wall boundary layer to obtain satisfactory far-field noise predictions.

Recently, high-order discontinuous methods, such as the discontinuous Galerkin (DG) method [28] and spectral difference (SD) method [29] have been applied to computational fluid dynamics (CFD). These methods approximate solutions using piecewise continuous high-order polynomials in the computational domain to achieve high-order of accuracy on an unstructured mesh. The compact stencil of these methods make them more efficient for parallelization. These high-order methods were implemented in codes such as the Jet Engine Noise Reduction (JENRE) code [30] and Glenn Flux Reconstruction (GFR) code [31] to simulate the supersonic jet noise. Validation showed that accurate results can be achieved on a much coarser grid relative to the grid required by the finite volume solvers.

Proper Orthogonal Decomposition (POD) was first introduced by Lumley [32] to the fluid dynamics community and became one of the most widely used methods to extract coherent structures from turbulent flows. POD aims to extract optimal modes that can efficiently capture the energy or \mathcal{L}_2 norm of the selected variables. The original method of Lumley [32] uses a space-time formulation, which produces spatial-temporal coherent modes. However, due to the limited temporal resolution of particle image velocimetry (PIV) in the past, a space-only formulation of POD has become popular. This formulation collapses the time dependence of the data and produces only spatially coherent structures. Details of different types of POD are found in a review paper by Tiara et al. [33]. Recently, POD was applied to the near-field pressure of jets with both experimental [34] and simulation data [35]. Structures similar to the growing and decaying instability waves were observed. Gordeyev and Thomas [36] applied POD to the experimental data on different cross-stream planes to examine the self-similarity of the coherent structures of planar jets. Freund and Colonius [37] used POD to ascertain the norm that represents sound generating dynamics.

B. Present Approach

In the present work, we perform LES of an under-expanded heated supersonic jet. The simulation is validated using aerodynamic and acoustic results. The aerodynamic results are compared with a RANS simulation at the same jet operating condition. The acoustic predictions are calculated using the FWH acoustic solver and compared with the experimental data from NASA’s Small Hot Jet Acoustic Rig (SHJAR) [38] database.

Miller [39] proposed an acoustic analogy based on the decomposition of Navier-Stokes equations. The Navier-Stokes equations are decomposed into a time averaged base flow, aerodynamic turbulent fluctuations, and acoustic fluctuations. The aerodynamic fluctuations are in turn decomposed into fluctuations from large-scale turbulence and fine-scale turbulence. The acoustic fluctuations are calculated using the vector Green’s function and the two-point cross-correlation of the equivalent sources. These sources can be evaluated either using turbulence theories or from numerical simulations.

We follow the methodology of Miller [39] to identify the noise sources associated with shock wave turbulence interactions in the jet shear layer. The BBSAN source is obtained using LES data. We apply POD to decompose the simulated velocity field into spatial-temporal modes that represent different scales of turbulent structures in the jet flow. The BBSAN spectra at different observation angles are calculated using both complete and reconstructed flow-fields to identify the most acoustically efficient modes for BBSAN. Next, the source intensity distribution is plotted to identify the major source locations. Finally, we plot the two-point space-time cross-correlation of the source term and compare with the empirical model by Ribner [40] to study the source statistics and show the advantage of the present method over the RANS based methods.

II. Methodology

A. Governing Equations

The flow-field is modeled by the the Favre filtered Navier-Stokes equations,

$$\frac{\partial \bar{\rho}}{\partial t} + \frac{\partial \bar{\rho} \tilde{u}_j}{\partial x_j} = 0, \quad (1)$$

$$\frac{\partial}{\partial t} (\bar{\rho} \tilde{u}_i) + \frac{\partial}{\partial x_j} \left[\bar{\rho} \tilde{u}_i \tilde{u}_j + \bar{p} \delta_{ij} - \tilde{\tau}_{ij}^{tot} \right] = 0, \quad (2)$$

and

$$\frac{\partial}{\partial t} (\bar{\rho} \tilde{e}_0) + \frac{\partial}{\partial x_j} \left[\bar{\rho} \tilde{u}_j \tilde{e}_0 + \tilde{u}_j \bar{p} + \tilde{q}_j^{tot} - \tilde{u}_i \tilde{\tau}_{ij}^{tot} \right] = 0, \quad (3)$$

where $\bar{\rho}$, \tilde{u}_i , and \tilde{e}_0 are the Reynolds averaged density, Favre averaged velocity components, and Favre averaged specific total energy, respectively. $\tilde{\tau}^{tot} = \tilde{\tau} + \tilde{\tau}^{sgs}$ and $\tilde{q}^{tot} = \tilde{q} + \tilde{q}^{sgs}$ are the total viscous stress and total heat flux, which are composed of resolved and sub-grid scale components. The Favre averaged viscous stress and heat flux are

$$\tilde{\tau}_{ij} = 2\mu \left(\tilde{S}_{ij} - \frac{1}{3} \tilde{S}_{mm} \delta_{ij} \right), \quad (4a)$$

$$\tilde{q}_j = -\gamma \left(\frac{\mu}{Pr} \right) \frac{\partial \tilde{e}}{\partial x_j}, \quad (4b)$$

where

$$S_{ij} = \frac{1}{2} \left(\frac{\partial u_i}{\partial x_j} + \frac{\partial u_j}{\partial x_i} \right). \quad (4c)$$

The sub-grid scale viscous stress and heat flux are modeled as

$$\tilde{\tau}_{ij}^{sgs} = 2\mu_t \left(\tilde{S}_{ij} - \frac{1}{3} \tilde{S}_{mm} \delta_{ij} \right) - \frac{2}{3} \bar{\rho} k \delta_{ij} \quad (5a)$$

and

$$\tilde{q}_j^{sgs} = -\gamma \left(\frac{\mu_t}{Pr_t} \right) \frac{\partial \tilde{e}}{\partial x_j}, \quad (5b)$$

where $\frac{2}{3} \bar{\rho} k \delta_{ij}$ is neglected since its contribution is small [41]. The turbulent Prandtl number $Pr_t = 0.9$ and the eddy viscosity μ_t are modeled using wall-adapting local eddy viscosity (WALE) model [42] as

$$\mu_t = \rho (C_w \Delta)^2 \frac{(S_{ij}^d S_{ij}^d)^{3/2}}{(\bar{S}_{ij} \bar{S}_{ij})^{5/2} + (S_{ij}^d S_{ij}^d)^{5/4}}, \quad (6)$$

where

$$S_{ij}^d = \frac{1}{2} \left(\bar{g}_{ij}^2 + \bar{g}_{ji}^2 \right) - \frac{1}{3} \delta_{ij} \bar{g}_{kk}^2, \quad (7)$$

$$\bar{g}_{ij}^2 = \frac{\partial \tilde{u}_i}{\partial x_k} \frac{\partial \tilde{u}_k}{\partial x_j}, \quad (8)$$

$C_w = 0.325$, and Δ is the filter width.

B. Numerical Methods

An open-source code called High Fidelity Large Eddy Simulation (HiFiLES) [43] is modified. HiFiLES is an unstructured high-order compressible Navier-Stokes solver. The solver uses Energy-Stable Flux Reconstruction schemes (ESFR) [44] to achieve high-order of accuracy. Compared to other high-order methods, this method unifies many existing approaches such as the discontinuous Galerkin (DG) scheme [28] and the spectral difference (SD) method [29] with a simplified implementation. The high-order of accuracy is achieved by using high-order polynomials to approximate the solution inside each element. A correction function is chosen to account for the common interface flux and reconstruct the flux inside the elements.

Due to the low dissipation and low dispersion nature of the schemes, explicit LES can be used to model the unresolved scales of turbulence. For simulations of supersonic flow, shocks can appear in the flow-field and lead to numerical instability. To avoid this, a shock capturing method is implemented to stabilize the solution inside of elements. In order to efficiently sample time-resolved flow-field data, a numerical probe is also implemented in the solver.

1. Spatial Discretization

The governing equations are written in the form of general conservation equation as

$$\frac{\partial \mathbf{q}}{\partial t} + \nabla \cdot \mathbf{F} = 0, \quad (9)$$

where \mathbf{q} is the solution vector and $\mathbf{F} = \mathbf{F}_{inv} + \mathbf{F}_{visc}$ is the total flux tensor. The computational domain is divided into non-overlapping elements, which conform to the boundaries. For simplicity, we transform each element into the reference domain. The transformation Jacobian is defined as

$$\mathbf{J} = \frac{\partial \mathbf{x}}{\partial \hat{\mathbf{x}}}, \quad (10)$$

where $\mathbf{x} = \mathbf{x}(\hat{\mathbf{x}})$ is the shape function.

The solution of Eq. (9) can be determined by solving the transformed equation

$$\frac{\partial \hat{\mathbf{q}}}{\partial t} + |\mathbf{J}|^{-1} \hat{\nabla} \cdot \hat{\mathbf{F}} = 0, \quad (11)$$

where $\hat{\mathbf{q}}(\hat{\mathbf{x}}, t) = \mathbf{q}(\mathbf{x}, t)$ and $\hat{\mathbf{F}}(\hat{\mathbf{x}}, t) = |\mathbf{J}| \mathbf{J}^{-1} \cdot \mathbf{F}(\mathbf{x}, t)$ are the transformed solution and flux, respectively. Inside the reference element, the solution and flux are approximated using a \mathcal{P}^{th} order polynomial. The polynomial is constructed through interpolation on a set of solution points in each element as

$$\hat{\mathbf{q}}^\delta(\hat{\mathbf{x}}) = \sum_{i=1}^{N_s} \hat{\mathbf{q}}^\delta(\hat{\mathbf{x}}_i) l_i(\hat{\mathbf{x}}), \quad (12a)$$

and

$$\hat{\mathbf{F}}^\delta(\hat{\mathbf{x}}) = \sum_{i=1}^{N_s} \hat{\mathbf{F}}^\delta(\hat{\mathbf{x}}_i) l_i(\hat{\mathbf{x}}), \quad (12b)$$

where the superscript δ represents the discontinuous solution or flux and N_s is the number of solution points in the element. On the interface flux points, a common numerical flux is required to recover a meaningful global solution. The normal common inviscid flux can be calculated using a Riemann solver given the discontinuous solutions at the left and right side of the interface. The Harten-Lax-van Leer-Contact (HLLC) [45] Riemann solver is implemented for this purpose. The normal common inviscid flux at the interface in the physical domain is written as

$$\mathbf{F}_{inv}^{\delta I \perp} = \mathcal{F}^{HLLC}(\mathbf{F}_{inv}^{\delta L}, \mathbf{F}_{inv}^{\delta R}, \mathbf{n}), \quad (13)$$

where $\mathbf{F}_{inv}^{\delta L}$ and $\mathbf{F}_{inv}^{\delta R}$ are the discontinuous inviscid flux at two sides of the interface and \mathbf{n} is the physical outward unit normal vector on the interface.

For the viscous flux, a DG method [46] is used. The process to calculate the viscous flux is similar to the inviscid flux, except that the gradients used to calculate the viscous flux are corrected via a correction function and the common interface solution. On each interface flux point, the common solution is evaluated by

$$\mathbf{q}^{\delta I} = \frac{1}{2} (\mathbf{q}^{\delta L} + \mathbf{q}^{\delta R}) - \beta (\mathbf{q}^{\delta L} - \mathbf{q}^{\delta R}), \quad (14)$$

where $\mathbf{q}^{\delta L}$ and $\mathbf{q}^{\delta R}$ are the discontinuous solution vectors on the two sides of the interface and β is the penalty factor. We choose

$$\beta = \frac{\mathbf{n} \cdot \mathbf{a}}{2|\mathbf{n} \cdot \mathbf{a}|} \quad (15)$$

to recover a local DG (LDG) scheme, where \mathbf{a} is an arbitrary reference unit vector to ensure consistency. We then correct the transformed gradients inside each element as

$$\hat{\nabla} \hat{\mathbf{q}}^{\delta C}(\hat{\mathbf{x}}) = \hat{\nabla} \hat{\mathbf{q}}^\delta(\hat{\mathbf{x}}) + \sum_{i=1}^{N_i} \sum_{j=1}^{N_f} \hat{\mathbf{n}}_{i,j} \hat{\nabla} \cdot \mathbf{g}_{i,j}(\hat{\mathbf{x}}) [\hat{\mathbf{q}}_{i,j}^{\delta I} - \hat{\mathbf{q}}_{i,j}^\delta], \quad (16)$$

where N_i is the number of interfaces and N_f is the number of flux points on each interface, so that $\mathbf{g}_{i,j}(\hat{\mathbf{x}})$ represents the correction function associated with the flux point j on interface i . In the present work, we choose the correction function to recover a nodal collocation-based DG scheme [47]. The corrected gradients in the reference domain are transformed back to the physical domain using

$$\nabla \mathbf{q}^{\delta C}(\mathbf{x}) = \mathbf{J}^{-T} \cdot \hat{\nabla} \hat{\mathbf{q}}^{\delta C}(\hat{\mathbf{x}}). \quad (17)$$

The normal common viscous flux on the interface can then be calculated using the solution and the corrected viscous flux as

$$\mathbf{F}_{visc}^{\delta I \perp} = \mathbf{n} \cdot \left[\frac{1}{2} (\mathbf{F}_{visc}^{\delta L} + \mathbf{F}_{visc}^{\delta R}) + \beta (\mathbf{F}_{visc}^{\delta L} - \mathbf{F}_{visc}^{\delta R}) \right] - \tau (\mathbf{q}^{\delta R} - \mathbf{q}^{\delta L}), \quad (18)$$

where $\tau = 0.1$ (see Castonguay et al. [48] for details) is the stabilization factor. Next, the normal common total flux in the physical domain is transformed into the reference domain using

$$\hat{\mathbf{F}}^{\delta I \perp} = |\mathbf{J}| \cdot |\mathbf{J}^{-T} \cdot \hat{\mathbf{n}}| \mathbf{F}^{\delta I \perp}. \quad (19)$$

The final semi-discretized equation can be written as

$$\frac{d\hat{\mathbf{q}}}{dt} = -|\mathbf{J}|^{-1} \left[\hat{\nabla} \cdot \hat{\mathbf{F}}^{\delta} + \sum_{i=1}^{N_i} \sum_{j=1}^{N_f} \hat{\nabla} \cdot \mathbf{g}_{i,j}(\hat{\mathbf{x}}) (\hat{\mathbf{F}}_{i,j}^{\delta I \perp} - \hat{\mathbf{F}}_{i,j}^{\delta \perp}) \right]. \quad (20)$$

2. Shock Capturing Method

Hesthaven and Kirby [49] connected the convergence rate of a function to the decay of its expansion coefficients. Persson [50] used this property as a shock indicator to capture discontinuities. We follow Persson's method, but apply it to the density field instead of entropy for simplicity. Recalling Parseval's theorem, the shock detector for each element can be written as

$$\epsilon = \frac{\Gamma_{N_s} \check{\rho}_{N_s}^2}{\sum_{i=1}^{N_s} \Gamma_i \check{\rho}_i^2}, \quad (21)$$

where

$$\check{\rho}_i = \sum_{j=1}^{N_s} \mathcal{V}_{ij}^{-1} \rho_j, \quad (22a)$$

$$\mathcal{V}_{ij} = \psi_j(\hat{\mathbf{x}}_i), \quad (22b)$$

and

$$\Gamma_i = \int \psi_i^2(\hat{\mathbf{x}}) d\hat{\mathbf{x}}. \quad (22c)$$

Here, $\check{\rho}$ is the modal coefficient of density, \mathcal{V} is the Vandermonde matrix that connects the modal and nodal space, and ψ_i is the i^{th} orthogonal polynomial basis in the reference domain. The shock detector is evaluated for all the elements at the end of each time step.

If the shock detector value in an element is higher than the threshold, an exponential filter will be applied to the modal coefficients of all the solution variables in that element to stabilize the solution. The modal exponential filter for an 1-D element is

$$\sigma_i = \exp \left[-\alpha \left(\frac{i}{\mathcal{P}} \right)^\zeta \right], \quad (23)$$

where α is the filter strength and ζ is the filter order. The filter can be readily extended to multi-dimensional elements. The filtered modal solutions are transformed back to the nodal values using

$$\mathbf{q}_i = \sum_{j=1}^{N_s} \sigma_j \check{\mathbf{q}}_j \mathcal{V}_{ij}. \quad (24)$$

According to Hesthaven and Kirby [49], the convergence rate of the solution around the discontinuities is affected by the order of the filter. Higher filter order will result in higher order of accuracy in the filtered element. We first determine the filter order ζ . Then the filter strength α is set accordingly to be strong enough to stabilize the solution. The threshold of the shock sensor should vary with the polynomial order of the simulation \mathcal{P} and has a scaling of \mathcal{P}^{-4} , suggested by Persson [50]. In the present work, a trial and error process is used to determine the threshold and the filter strength. First, the threshold is set to zero to ascertain the minimum value of α to stabilize the solution. Then, the threshold is determined by increasing its value until the simulation becomes unstable again.

The filtering procedure involves only one matrix multiplication. In addition, the present method does not require any communications with other processors, which simplifies the implementation and reduces the computational cost compared to other limiter based methods [51].

3. Numerical Probe

Flow-field analysis and acoustic prediction require time resolved data from the flow-field. As an alternative to storing the entire numerical solution, we implemented a numerical probe to extract time resolved data. Numerical probes are placed along lines, on surfaces, or inside of volumes within the flow-field for different purposes. The coordinates of the numerical probes are calculated by reading a descriptive script. After the element which each probe belongs to is determined through vector multiplications, the coordinates of the probes in the reference domain are found iteratively using Newton's method of root finding as

$$\hat{\mathbf{x}}_{n+1} = \hat{\mathbf{x}}_n - (\mathbf{x}_n - \mathbf{x}_p) / \mathbf{J}(\hat{\mathbf{x}}_n). \quad (25)$$

The iteration is considered converged if $\|\hat{\mathbf{x}}_{n+1} - \hat{\mathbf{x}}_n\|_\infty < 10^{-6}$ in the present work. Finally, as the simulation runs, the solution on probe points can be obtained by interpolation as

$$\mathbf{q}(\hat{\mathbf{x}}_p) = \hat{\mathbf{q}}(\hat{\mathbf{x}}_p) = \sum_{i=1}^{N_s} \hat{\mathbf{q}}(\hat{\mathbf{x}}_i) l_i(\hat{\mathbf{x}}_p). \quad (26)$$

C. Ffowcs Williams and Hawkings Method

Ffowcs Williams and Hawkings [18] proposed an integral method to calculate far-field noise based on Lighthill's acoustic analogy [52, 53]. This method uses flow-field information on an arbitrary shaped surface. The surface can be either solid or porous.

The FWH equation with a porous subsonic moving surface $f(\mathbf{x}, t) = 0$ is

$$\left(\frac{1}{c_\infty^2} \frac{\partial^2}{\partial t^2} - \frac{\partial^2}{\partial x_i^2} \right) [p' \mathcal{H}(f)] = \frac{\partial}{\partial t} [\rho_\infty U_n \delta(f)] - \frac{\partial}{\partial x_i} [L_i \delta(f)] + \frac{\partial^2}{\partial x_i \partial x_j} [T_{ij} \mathcal{H}(f)], \quad (27)$$

where

$$U_i = \left(1 - \frac{\rho_*}{\rho_\infty} \right) v_i + \frac{\rho_* u_i}{\rho_\infty}, \quad (28a)$$

$$L_i = p' \mathbf{n}_i + \rho_* u_i (u_n - v_n), \quad (28b)$$

and

$$\rho_* = \rho_\infty + p' / c_\infty^2. \quad (28c)$$

The ambient speed of sound and ambient density are represented by c_∞ and ρ_∞ , $T_{ij} = \rho u_i u_j + (p' - c_\infty^2 \rho') \delta_{ij}$ is the Lighthill's stress tensor, p' and $\rho' = \rho - \rho_\infty$ are the pressure and density perturbation, v_i are the surface velocity components, and the subscript n implies the dot product with unit surface normal vector. The use of ρ_* instead of ρ was reported by Spalart and Shur [54] to obtain better predictions for heated jets.

Farassat [55] solved the equation using a free-space Green's function of the wave equation. Assuming the surface is fixed in space ($v_i = 0$) and no sources are outside of the surface ($T_{ij} \mathcal{H}(f) = 0$), the solution of Eq. (27) is

$$p'(\mathbf{x}, t) = \frac{1}{4\pi} \int \left[\frac{\rho_\infty \dot{U}_n}{r} + \frac{\dot{L}_r}{c_\infty r} + \frac{L_r}{r^2} \right]_{sr c} dS. \quad (29)$$

The integrand is evaluated at source time, where $r = |\mathbf{x} - \mathbf{y}|$ is the distance between the source location \mathbf{y} to the observer location \mathbf{x} . The subscript r indicates the dot product with a unit vector in the source-observer direction. The $\dot{}$ indicates the derivative with respect to source time.

D. Decomposition of Navier-Stokes Equations

Miller [39] proposed an acoustic analogy based on the decomposition of Navier-Stokes equations. The field variables \mathbf{q} , including density, velocity, and pressure are decomposed into

$$\mathbf{q} = \overline{\mathbf{q}} + \mathbf{q}' + \hat{\mathbf{q}} + \check{\mathbf{q}}, \quad (30)$$

where the overline operator represents the time-averaged base flow, the check operator indicates the isotropic component, the hat operator indicates the anisotropic component, and a prime denotes the radiating component of the variable. The decomposed variables are substituted into the Navier-Stokes equations. The equations are rearranged such that the radiating quantities are on the left hand side, while the base flow and aerodynamic fluctuating quantities are brought to the right hand side. The left hand side terms are known as propagators and the right hand side terms are known as the equivalent sources. The source terms on the right hand side are

$$\Theta_0 = -\frac{\partial \underline{\rho}}{\partial t} - \frac{\partial \underline{\rho} \underline{u}_j}{\partial x_j}, \quad (31)$$

$$\Theta_i = -\frac{\partial \underline{\rho} \underline{u}_i}{\partial t} - \frac{\partial \underline{\rho} \underline{u}_i \underline{u}_j}{\partial x_j} - \frac{\partial \underline{p}}{\partial x_j} \delta_{ij} + \frac{\partial}{\partial x_j} \left[\mu \left(\frac{\partial \underline{u}_i}{\partial x_j} + \frac{\partial \underline{u}_j}{\partial x_i} \right) \right] - \frac{2}{3} \frac{\partial}{\partial x_j} \left[\mu \frac{\partial \underline{u}_k}{\partial x_k} \right], \quad (32)$$

and

$$\begin{aligned} \Theta_4 = & -\frac{\partial \underline{p}}{\partial t} - \frac{\gamma - 1}{2} \frac{\partial \underline{\rho} \underline{u}_k \underline{u}_k}{\partial t} - \gamma \frac{\partial \underline{u}_j \underline{p}}{\partial x_j} - \frac{\gamma - 1}{2} \frac{\partial \underline{\rho} \underline{u}_j \underline{u}_k \underline{u}_k}{\partial x_j} + (\gamma - 1) \frac{\partial}{\partial x_j} \left[\frac{c_p \mu}{Pr} \frac{\partial T}{\partial x_j} \right] + (\gamma - 1) \frac{\partial}{\partial x_j} \left[\mu \underline{u}_i \left(\frac{\partial \underline{u}_i}{\partial x_j} + \frac{\partial \underline{u}_j}{\partial x_i} \right) \right] \\ & - \frac{2}{3} (\gamma - 1) \delta_{ij} \frac{\partial}{\partial x_j} \left[\mu \underline{u}_i \frac{\partial \underline{u}_k}{\partial x_k} \right], \end{aligned} \quad (33)$$

where Θ_0 represents the source terms from the continuity equation, Θ_i (where $i = 1, 2, 3$) represents the three components of the source terms from momentum equations, and Θ_4 represents the source terms from the energy equation. The under-bar operator from Eq. (31) to (33) denote the sum of the base quantity and fluctuating quantities, i.e. $\underline{q} = \overline{q} + \hat{q} + \check{q}$.

The spectral density of radiating acoustic pressure is

$$S(\mathbf{x}, f) = \int_{-\infty}^{\infty} \dots \int_{-\infty}^{\infty} \sum_{m=0}^4 \sum_{n=0}^4 \hat{g}_{p,m}(\mathbf{x}, \mathbf{y}; f) \hat{g}_{p,n}^*(\mathbf{x}, \mathbf{z}; f) R_{m,n}(\mathbf{y}, \mathbf{z}, \Delta\tau) \exp[-i2\pi f \Delta\tau] d\Delta\tau dz dy, \quad (34)$$

where \hat{g}_p is the Fourier transformed vector Green's function of acoustic pressure, \mathbf{x} is the observer location, and \mathbf{y} and \mathbf{z} are the source locations. Equation (34) is composed by convolution of the Fourier transformed two-point cross-correlations between the source terms and the Fourier transformed vector Green's function. The two-point space-time cross-correlation in Eq. (34) denoted by $R_{m,n}(\mathbf{y}, \mathbf{z}, \tau)$ is written as

$$R_{m,n}(\mathbf{y}, \mathbf{z}, \Delta\tau) = \int_{-\infty}^{\infty} \Theta_m(\mathbf{y}, \tau + \Delta\tau) \Theta_n(\mathbf{z}, \tau) d\tau, \quad (35)$$

where $\Delta\tau$ is the time delay between the two sources.

Since the acoustic analogy is based on the decomposition of the Navier-Stokes equations, all the noise sources should be present on the right hand side as source terms. Based on the physics and scaling analysis of the shock-associated noise, Patel and Miller [56] identified the source term responsible for shock-associated noise. The source term for shock-associated noise is

$$\Theta_s = -\gamma \hat{u}_j \frac{\partial \overline{p}}{\partial y_j}, \quad (36)$$

which is the scalar product of mean pressure gradient and anisotropic velocity. Here, the gradient of mean pressure denotes the shock-strength while the anisotropic velocity represents the large-scale turbulent structures. The source term for fine-scale mixing noise used by Tam [57] is also obtained from the source terms using this acoustic analogy without any further rearrangement. Potential source terms for large-scale mixing noise are also present within the acoustic analogy.

To evaluate the source term of BBSAN, the velocity fluctuations associated with large-scale structures have to be extracted from the total fluctuations. In the work of Patel and Miller [56], the anisotropic velocity was modeled using theoretical and experimental results. In the current work, we use POD to decompose the time-resolved flow-field obtained from LES to obtain velocity fluctuations of large-scale turbulent structures. This removes some of the empiricism associated with modeling the isotropic and anisotropic velocity.

E. Proper Orthogonal Decomposition

The objective of POD is to extract optimal modes that are coherent in space and time. According to Lumley [32], this procedure is equivalent to solving the following eigenvalue problem

$$\iint C(\mathbf{x}, \mathbf{x}'; t, t') \phi(\mathbf{x}', t') d\mathbf{x}' dt' = \lambda \phi(\mathbf{x}, t), \quad (37)$$

where

$$C(\mathbf{x}, \mathbf{x}'; t, t') = E\{\mathbf{q}(\mathbf{x}, t)\mathbf{q}^*(\mathbf{x}', t')\} \quad (38)$$

is the cross-correlation tensor of input vector data $\mathbf{q}(\mathbf{x}, t)$, the asterisk represents the complex conjugate, and $E\{\cdot\}$ represents the ensemble average over different realizations of the flow. The resulting modes $\phi(\mathbf{x}, t)$ are orthogonal and the eigenvalues λ represent the average amount of energy extracted by these modes. For stationary flow, the cross-correlation tensor reduces to $C(\mathbf{x}, \mathbf{x}'; \tau)$. Using the Wiener-Khinchin theorem, the cross-correlation tensor is Fourier transformed to obtain the cross-spectral density tensor as

$$S(\mathbf{x}, \mathbf{x}'; f) = \int C(\mathbf{x}, \mathbf{x}'; \tau) e^{-i2\pi f \tau} d\tau. \quad (39)$$

Then Eq. (37) can be written for each frequency component as

$$\int S(\mathbf{x}, \mathbf{x}'; f) \phi(\mathbf{x}', f) d\mathbf{x}' = \lambda(f) \phi(\mathbf{x}, f). \quad (40)$$

We now show the steps to compute POD from simulation data. Following Towne et al. [58], the input data can be expressed in matrix form as

$$\mathbf{Q} = \begin{bmatrix} \mathbf{q}_1 & \mathbf{q}_2 & \dots & \mathbf{q}_N \end{bmatrix} \in \mathbb{R}^{M \times N}, \quad (41)$$

where each column represents a snapshot of the flow-field and N snapshots are sampled with time step size Δt . Using Welch's method [59], the data is first segmented into partially overlapping blocks. Each block is considered as one realization of the flow. Assuming each block contains N_f snapshots and N_o snapshots overlap between neighboring blocks, the total number of blocks can be calculated using $N_b = (N - N_o)(N_f - N_o)^{-1}$. Next, the windowed discretized Fourier transform for each block is computed using

$$\hat{\mathbf{Q}}^{(l)} = \begin{bmatrix} \hat{\mathbf{q}}_1^{(l)} & \hat{\mathbf{q}}_2^{(l)} & \dots & \hat{\mathbf{q}}_{N_f}^{(l)} \end{bmatrix} \in \mathbb{R}^{M \times N_f}, \quad (42a)$$

where

$$\hat{\mathbf{q}}_k^{(l)} = \sum_{j=1}^{N_f} \omega_j \mathbf{q}_j^{(l)} e^{-2\pi i(j-1)(k-1)/N_f}. \quad (42b)$$

Here, l is the block index and ω_j is the window function evaluated at point j . In the present work, a Hanning window is used, which is $\omega_j = 1/2[1 - \cos(2\pi(j-1)(N_f-1)^{-1})]$. The cross-spectral density matrix at frequency f_k is calculated using

$$\mathbf{S}_{f_k} = \frac{1}{\left(\sum_{j=1}^{N_f} \omega_j^2\right) N_f N_b} \sum_{l=1}^{N_b} \hat{\mathbf{q}}_k^{(l)} \left(\hat{\mathbf{q}}_k^{(l)}\right)^*. \quad (43)$$

Equation (43) can be rewritten into a compact form with the help of a new data matrix

$$\hat{\mathbf{Q}}_{f_k} = \sqrt{\frac{1}{N_f \sum_{j=1}^{N_f} \omega_j^2}} \left[\hat{\mathbf{q}}_k^{(1)}, \hat{\mathbf{q}}_k^{(2)}, \dots, \hat{\mathbf{q}}_k^{(N_b)} \right] \in \mathbb{R}^{M \times N_b}, \quad (44)$$

then Eq. (43) becomes

$$\mathbf{S}_{f_k} = \frac{1}{N_b} \hat{\mathbf{Q}}_{f_k} \hat{\mathbf{Q}}_{f_k}^*. \quad (45)$$

Finally, the eigenvalues and eigenvectors are calculated using eigenvalue decomposition

$$\mathbf{S}_{f_k} \mathbf{W} \mathbf{\Phi}_{f_k} = \mathbf{\Phi}_{f_k} \mathbf{\Lambda}_{f_k}, \quad (46)$$

where the $\mathbf{W} \in \mathbb{R}^{M \times M}$ is the quadrature weight tensor, which is non-zero only for the diagonal elements, $\mathbf{\Phi}_{f_k}$ is a unitary matrix, of which the columns are POD modes, and $\mathbf{\Lambda}_{f_k}$ is a diagonal matrix with eigenvalues corresponding to the extracted modes ranked in descending order.

To save computation time, the modes are usually calculated by directly performing singular value decomposition [33] of Eq. (44), which is

$$\sqrt{\mathbf{W}/N_b} \hat{\mathbf{Q}}_{f_k} = \left(\sqrt{\mathbf{W}} \mathbf{\Phi}_{f_k} \right) \mathbf{\Sigma}_{f_k} \mathbf{\Psi}_{f_k}^*, \quad (47)$$

where columns of $\mathbf{\Phi}_{f_k}$ contain the first N_b eigenvectors of \mathbf{S}_{f_k} and $\mathbf{\Sigma}_{f_k}$ is a diagonal matrix containing the corresponding eigenvalues. After the modes are obtained, the flow-field can be recovered using a truncated expansion

$$q^{(l)}(\mathbf{x}, k \Delta t) = \sum_{m=1}^{N_f} \sum_{n=1}^{N_m} a_{mn}^{(l)} \mathbf{\Phi}_{mn} e^{2\pi i(m-1)(k-1)/N_f}, \quad (48)$$

where N_m is the number of modes used for the reconstruction. a_{mn} is the coefficient associated with the n^{th} mode and the m^{th} frequency component. This coefficients can be calculated using the inner product of the eigenvectors and the data matrix as

$$\mathbf{a}_{f_k}^* = \hat{\mathbf{Q}}_{f_k}^* \mathbf{\Phi}_{f_k}. \quad (49)$$

III. Results

A. Simulation Setup

An under-expanded heated supersonic jet test case is selected from NASA's SHJAR database. A baseline small metal chevron (SMC000) converging nozzle designed by NASA Glenn Research Center is used in the present work. The nozzle exit diameter is $D = 0.0508$ m with a lip thickness of $0.025D$. Table 1 shows the jet parameters, where the subscript o represents total conditions, the subscript ∞ represents ambient conditions, and Re_D is the Reynolds number based on the nozzle diameter.

p_o/p_∞	T_o/T_∞	T_j [K]	M_j	u_j [m/s]	Re_D
3.514	3.2	670.4	1.47	762.39	6.26×10^5

Table 1 Simulation Conditions.

1. Computational Domain and Mesh

The computational domain is shown in Fig. 1. The domain is a conical frustum with a radius of $r/D = 30$ at $x/D = -6$ and $r/D = 37.5$ at $x/D = 60$. The origin of the domain is located at the center of the nozzle exit plane. The nozzle geometry is included in the domain.

Tetrahedra elements are used in the current study for simplicity. A schematic of the computational mesh is shown in Fig. 2. In the region outlined by the blue lines, where the jet flow develops, the grid is refined to ensure a high resolution. The maximum mesh spacing Δx in this region grows from $0.025D$ at the nozzle exit to $0.35D$ at $x/D = 25$.

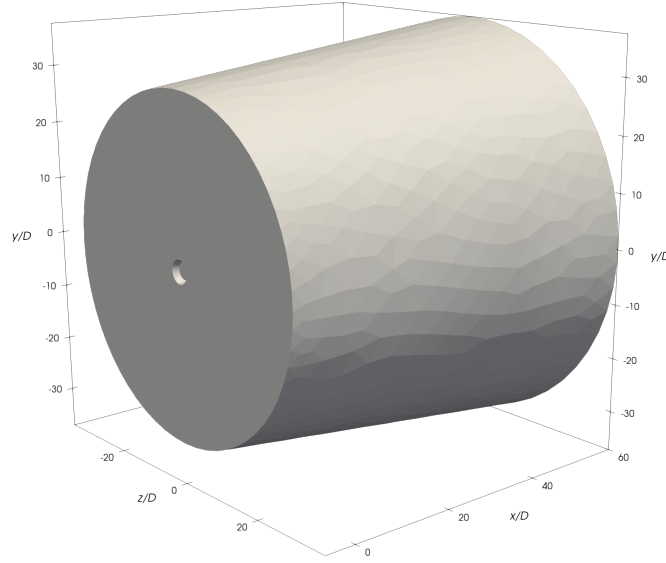


Fig. 1 Computational Domain.

The divergence rate of this region follows the spreading rate of the jet exhaust and includes the whole turbulent shear layer. In the jet near-field outlined by the region between the blue lines and the red lines, the grid is refined with a moderate grid spacing from $0.15D$ to $0.45D$ to capture the propagating acoustic waves for the FWH acoustic solver. The divergence rate of this region is slightly larger than the spreading rate of the jet flow considered in this paper.

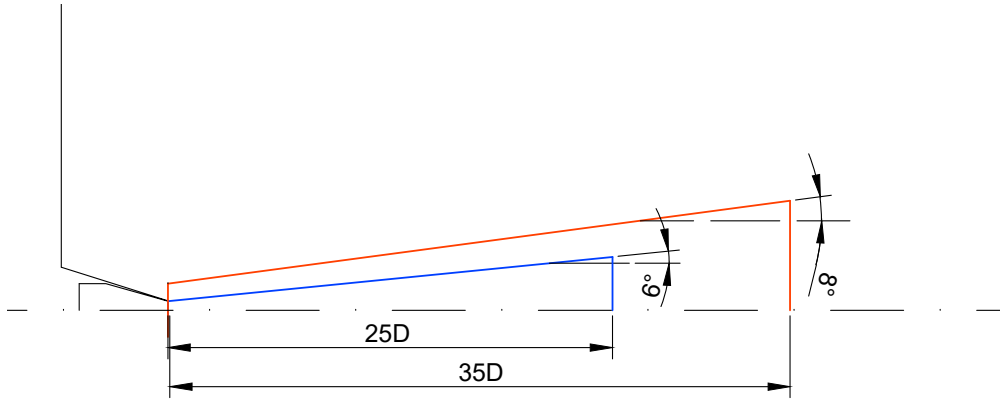


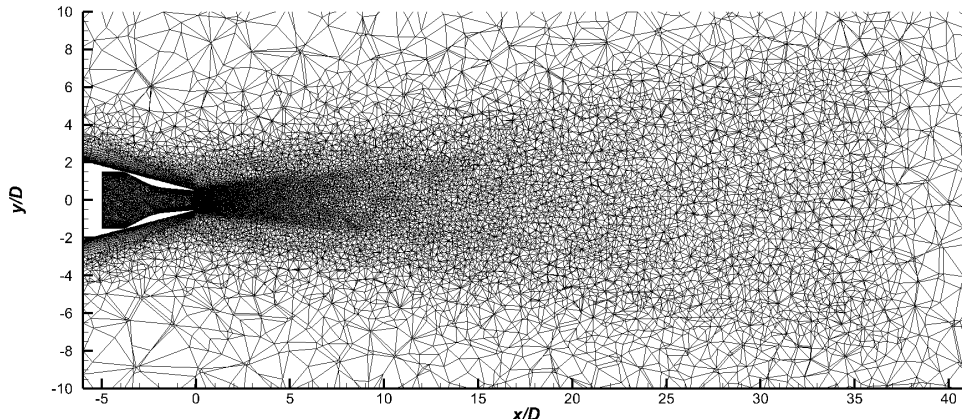
Fig. 2 Schematic of computational mesh.

Nyquist sampling criterion suggests that a signal contains frequencies no higher than f_{max} can be fully resolved with a sampling frequency of $2f_{max}$, where f_{max} is called the Nyquist frequency. However, energy from the unresolved scales reside near the Nyquist frequency in LES, resulting in an aliasing error. Brès and Nichols [60] recommended using eight points per wavelength to resolve an acoustic wave for LES of jet flow. Therefore, the highest resolved Strouhal number predicted by this criteria is

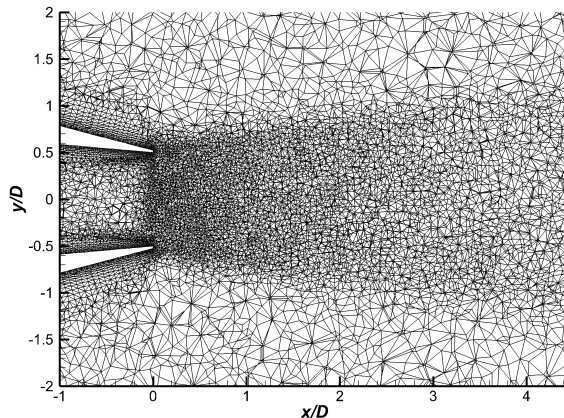
$$St_{max} = \frac{(\mathcal{P} + 1)c_{\infty}D}{8\Delta x u_j}. \quad (50)$$

If we run the simulation with a third-order polynomial, the current mesh can resolve up to $St = 1.5$ in the near-field mesh refinement region. The mesh is coarsened outside the jet exhaust region to reduce the computational cost.

Figure 3(a) shows a slice of the computational mesh at $z/D = 0$, while Fig. 3(b) shows an enlarged view near the nozzle exit. On the nozzle internal wall, in order to resolve a turbulent boundary layer, the first anisotropic layer must have a thickness of $\Delta y/D = 3.6 \times 10^{-5}$, which corresponds to $y^+ = 1$. However, this will lead to most of the elements being placed in the boundary layer and greatly reduces the CFL limit, which is contradictory to the purpose of using LES. Therefore, we set the first layer thickness to be $\Delta y/D = 0.01$ on the nozzle internal wall, corresponding to $y^+ = 280$.



(a) $z/D = 0$ slice of the mesh



(b) Enlarged view near nozzle exit

Fig. 3 Computational mesh.

The shape of the elements is isotropic far from the nozzle walls in the free-stream. This helps reduce spurious noise introduced by grid stretching as reported by Brès et al. [60]. In order to reduce the computational expense, the mesh is coarsened outside the refinement regions. This strategy does not reduce the accuracy of the acoustic prediction because the FWH surface is placed within the near-field refinement region of the mesh. The computational mesh consists of approximately 2.5 millions elements.

2. Boundary Condition

The internal and exterior walls of the nozzle are set as adiabatic non-slip walls. The flow-field is initialized with ambient conditions as $M_\infty = 10^{-4}$, $T_\infty = 300$ K, and $p_\infty = 101325$ Pa. At the nozzle inlet, a characteristic based subsonic inlet boundary condition is specified using total pressure and total temperature calculated with ambient conditions and jet parameters shown in Table. 1. To avoid any spurious reflections from the boundaries, Riemann invariant far-field

conditions are used for all external boundaries of the flow.

3. FWH Surface

In HiFiLES, the FWH surface is implemented using numerical probes, where each probe represents a triangular element on the surface. In the present work, the FWH surface is defined following the work of Mendez et al. [61]. The FWH surface is axisymmetric with a radius at the nozzle exit of $R(x/D = 0) = 1.5D$ and has an axial divergence rate of 0.2 to include the turbulent flow region. The surface terminates at $x/D = 35$ in the downstream direction, while in the upstream direction of the nozzle outlet, the surface extends to the left boundary of the domain, which follows the geometry of the nozzle exterior wall. Shur et al. [62] found that an end cap averaging technique can be used to eliminate low frequency spurious noise caused by turbulent structures exiting from the downstream side of the surface. Following their work, 11 evenly spaced end caps are placed between $x/D = 29$ and $x/D = 35$. The end caps are able to reduce spurious noise from $St = 0.008$ to 0.08. The placement of the FWH surface with end caps is shown in Fig. 4 with contour of x -momentum as the background to highlight the noise sources. It can be seen from Fig. 4 that the FWH surface is completely placed in the acoustic near-field, while most of the turbulent fluctuations are enclosed within the FWH surface.

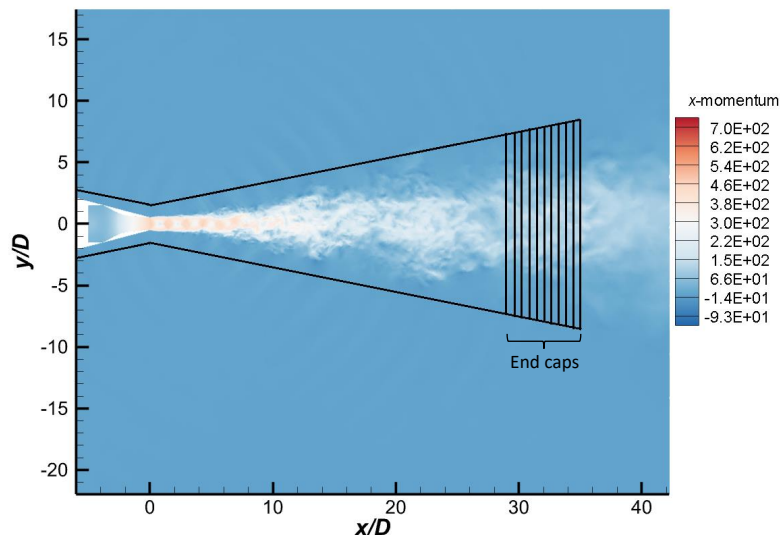


Fig. 4 Placement of FWH surface.

B. Simulation Results

In this section, we present the aerodynamic and acoustic results of the simulated jet. The time step size of the simulation is $\Delta t/t_{ref} = 1.5 \times 10^{-4}$, where $t_{ref} = R/c_\infty$ is the reference time. The data is sampled every $0.075t_{ref}$ for flow-field data on the lip-line and centerline, acoustic predictions, and BBSAN source analysis, resulting in a maximum accessible Strouhal number $St = 6.5$.

1. Aerodynamic Results

Figure 5 shows the instantaneous pressure field. At the nozzle exit, semi-periodic shock-cells are formed due to the pressure mismatch at the nozzle exit. The pressure in the near-field is dominated by downstream propagating acoustic waves. As observed by Liu et al. [63], the acoustic waves radiated near the nozzle exit have the largest wavenumber. Mach wave radiation propagating downstream with parallel patterns is observed. According to Tam [64], Mach wave radiation is generated by large-scale structures convecting with supersonic phase speed in the shear layer.

Figure 6 shows the comparison of mean axial velocity between the LES and RANS simulation. The RANS results are produced using FLUENT [65]. The RANS equations are closed using the Menter $k - \omega$ shear stress transport (SST) model [66]. A compressibility correction [67] and production limiter [68] are enabled.

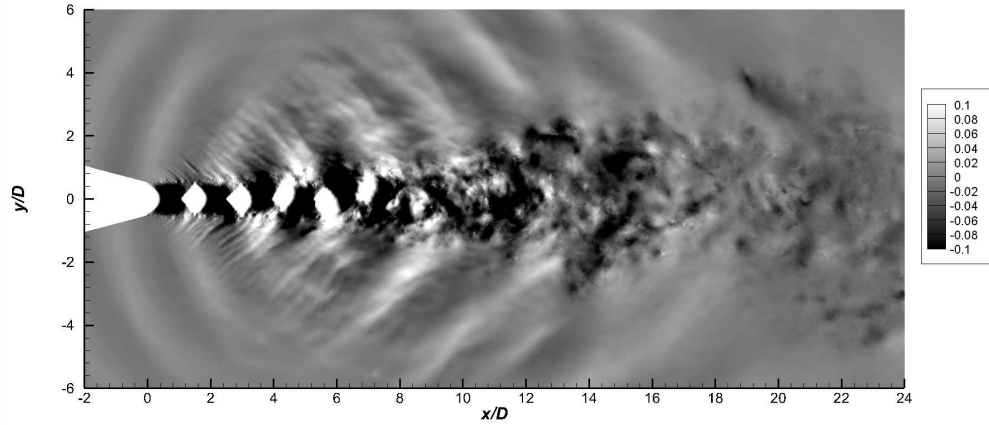


Fig. 5 Instantaneous fluctuating pressure $(p - p_\infty)p_\infty^{-1}$.

LES centerline mean axial velocity starts to decay at $x/D = 7$, while in the RANS solution this location is $x/D = 10$. Assuming that the potential core length can be calculated from the distance between $x/D = 0$ and position where $u/u_j = 0.95$, the potential core length predicted by LES is approximately $7.5D$. Similar results are produced by Georgiadis et al. [69] in their comparison of simulations and experiments. They showed that RANS always overestimates potential core length.

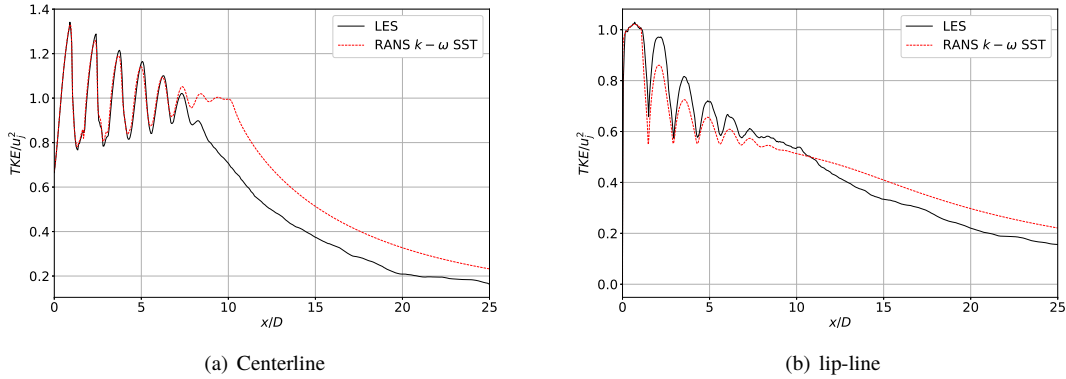


Fig. 6 Comparison of mean axial velocity between LES and RANS.

Figure 7 shows the comparison of the turbulent kinetic energy (TKE) between the LES and RANS simulations. Both simulations capture similar overall trends. However, LES produces larger maximum values of TKE along both the lip-line and centerline. TKE of LES is modulated by peaks along the lip-line and centerline due to the existence of the shock cells. The peak magnitude becomes increasingly large as the flow progresses downstream, which implies that the shock waves become increasingly unstable. This phenomenon is completely absent in the RANS results. At the nozzle exit, TKE is approximately zero along the lip-line for both simulations. As the flow progresses downstream, the TKE grows much faster along the lip-line than centerline, reaching its maximum value near the end of the potential core.

Power spectral density (PSD) of the axial velocity at several positions along the lip-line is presented in Fig. 8, which shows the spatial evolution of the jet shear layer. The spectrum at $x/D = 1$ just downstream of the nozzle outlet shows typical features of a transitional shear layer. The peaks in its spectrum represents the vortex roll-up and pairing effect due to the Kelvin-Helmholtz instability as suggested by Lele [70]. At $x/D = 7.5$, where the flow has become fully turbulent, the spectrum follows Kolmogorov's law with dominant low frequency components and a slope of $St^{-5/3}$ in the inertial subrange. As the probe moves to further downstream locations, the range of inertial subrange shifts to a lower frequency

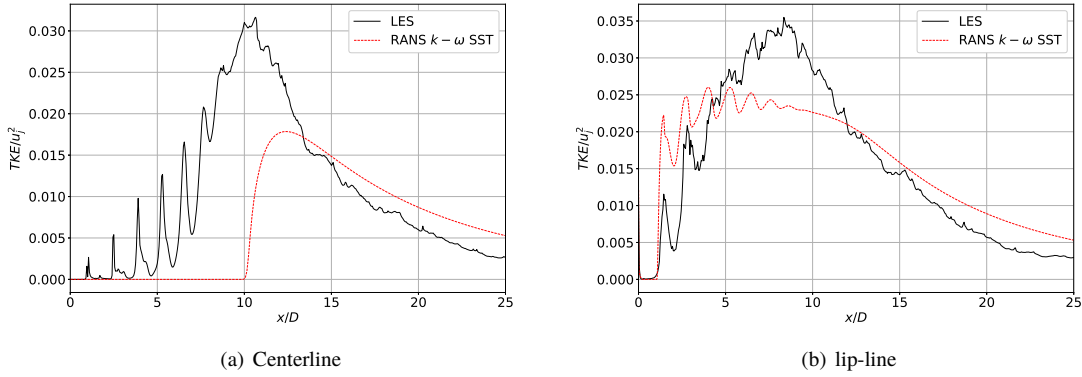


Fig. 7 Comparison of turbulent statistics between LES and RANS.

as observed by Liu et al. [71]. This suggests that the turbulent scales become larger as flow moves downstream. On the other hand, the dissipation range characterized by the quick drop in PSD, where TKE dissipates into internal energy, also shifts to lower frequency as the probe position moves downstream. This is due to the relatively larger grid spacing in the downstream region. The resolved Strouhal numbers calculated with Eq. (50) and the local speed of sound at $x/D = 7.5, 15,$ and 20 are $1.89, 0.80,$ and $0.67,$ respectively. These approximations agree well with the dissipation ranges in Fig. 8.

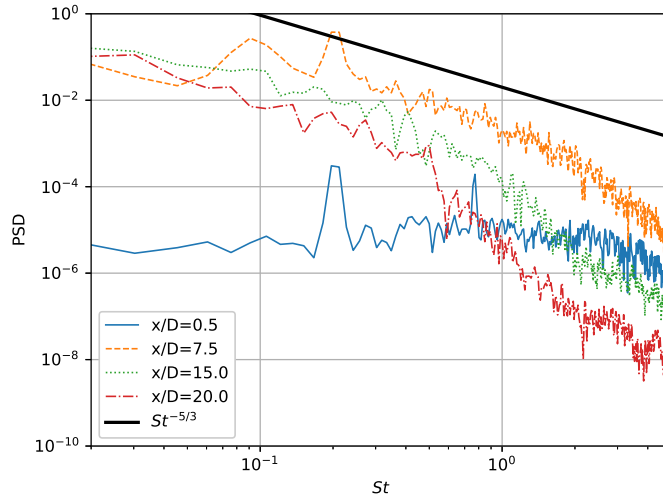


Fig. 8 Power spectrum of fluctuating axial velocity at different positions along the lip-line.

2. Acoustic Prediction

The experimental data is measured using a microphone array on an arc with a radius of $50D$ and scaled to $100D$ using lossless conditions [72]. The predictions are carried out using 3500 time samples on the FWH surface. The calculated spectra have poor statistical convergence, especially at low frequencies. In order to obtain smooth spectra, the solution from the FWH solver at 12 evenly spaced azimuthal locations are used and the spectra are averaged to obtain the noise spectrum for each observation angle.

Figure 9 shows comparisons of acoustic predictions relative to measurement at four representative observation angles, where ϕ is the angle relative to the downstream direction. The spectra are plotted from $St = 0.014$ to $St = 3$. At all angles, the predicted noise decays rapidly for $St \geq 1.5$, which is consistent with our estimation of the highest resolved

frequency based on grid resolution. At $\phi = 40^\circ$ relative to the jet downstream direction (Fig. 9(a)), where large-scale turbulent mixing noise is dominant, the prediction from LES shows good agreement with the experimental data with deviation less than 1 dB for $St > 0.08$. The discrete screech tone at $St = 0.2$ is also well captured in terms of frequency and amplitude. This result implies that our simulation is capable to accurately resolve large-scale turbulent motions in the flow-field.

At $\phi = 70^\circ$ (Fig. 9(b)), where the acoustic field is dominated by fine-scale mixing noise, a maximum 8 dB over-prediction by the LES is observed between $St = 0.06$ and $St = 0.7$. The over-estimation of the fine-scale noise can be attributed to the coarse grid resolution used by the current simulation as the small turbulent scales are not properly resolved. Moreover, the non-turbulent shear layer at the nozzle exit, according to Bogey et al. [73], will also introduce additional noise radiation at low frequencies, which mainly propagates between $\phi = 60^\circ$ to 90° . The screech tone at this angle is also not predicted. This is probably because the screech noise is masked by the over-predicted turbulent mixing noise.

At upstream angles (Fig. 9(c) and 9(d)), the noise spectrum is dominated by BBSAN. The peak of BBSAN moves to a lower peak frequency as the observer moves further upstream. The prediction from LES results show reasonable agreements with the experimental data with maximum error of 3 dB for $St \geq 0.1$. The shape and the frequency of the peak are well captured.

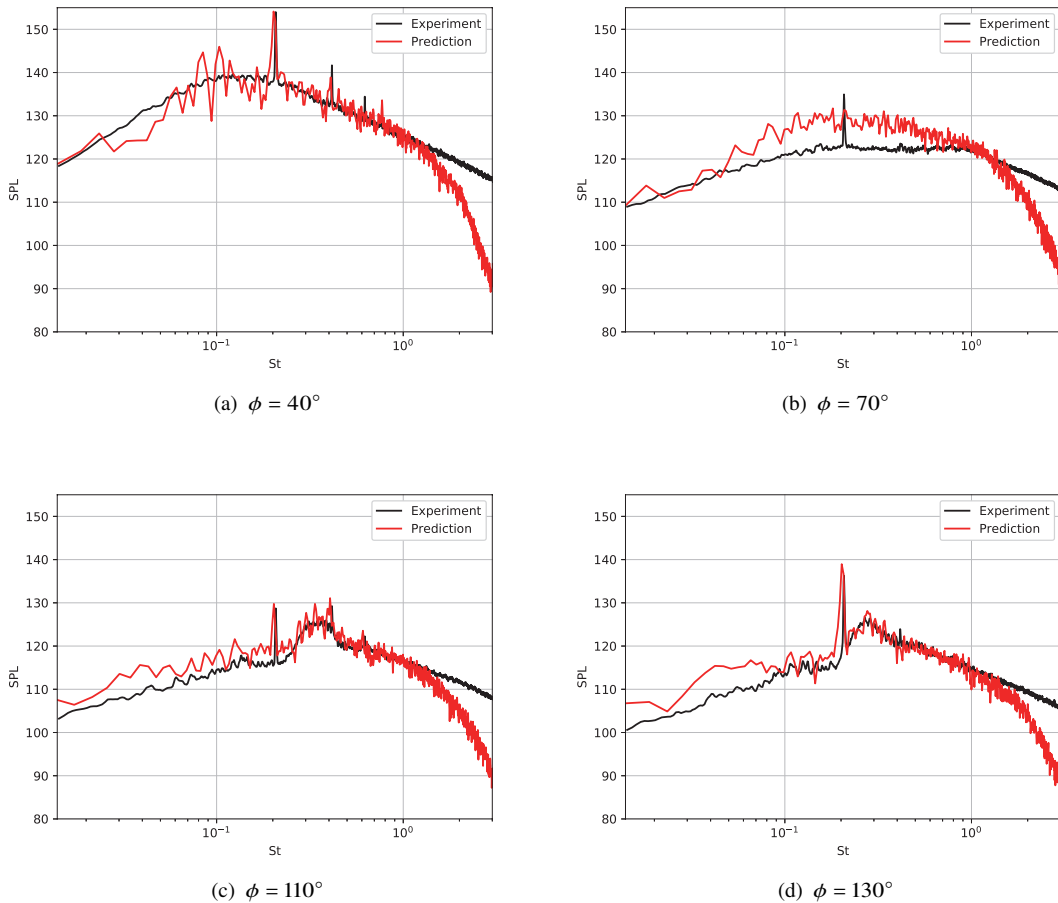


Fig. 9 Comparison of noise spectra between prediction and experiment.

C. Proper Orthogonal Decomposition

After the simulation is validated, we use its flow-field data to analyze the noise source of BBSAN. Recall that in Section II.D, the BBSAN source term identified from the decomposed Navier-Stokes equations is composed of the product of large-scale velocity fluctuations and the mean pressure gradient. Hence, we use the velocity vector for the decomposition, so that the POD modes represent the turbulent structures of different scales. Data are sampled in a cuboid volume, of which the dimensions are $x/D \in [0.1, 13]$, $y/D \in [-3, 3]$, and $z/D \in [-3, 3]$. The probes are uniformly distributed inside the volume, with a spacing between each probe $\Delta x/D = \Delta y/D = \Delta z/D = 0.1$. A diagram of the POD sampling volume with x -momentum as the background is presented in Fig. 10. The sampled data is divided into 12 partially overlapping blocks, each containing 512 snapshots with 256 overlapping snapshots between adjacent blocks. After the data division, mean values are subtracted from each block before the modes are computed.

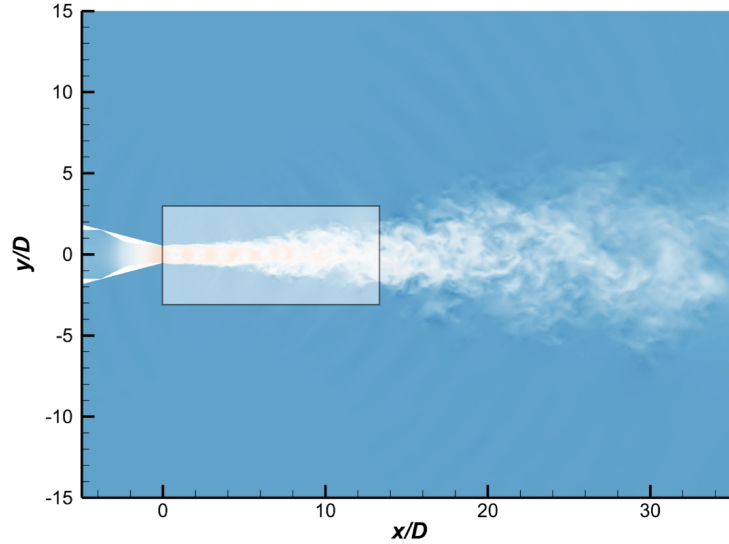


Fig. 10 Diagram of POD sampling volume.

Eigenvalues of the POD modes are plotted in Fig. 11 to show how the modal energy changes as a function of Strouhal number and mode number, where each line represents one POD mode. As the mode number increases, the line becomes increasingly transparent. Contributions of negative Strouhal numbers are added to the corresponding positive Strouhal numbers. In Fig. 11(a), eigenvalues are normalized by the summation of all eigenvalues, so that it represents the percentage of the energy extracted by each mode from the total energy. Alternatively, the eigenvalues at each Strouhal number are normalized independently by the summation of eigenvalues at the corresponding Strouhal number in Fig. 11(b). For all frequency components, the first mode always contains the most energy. Less energy is extracted as mode number increases.

At $St = 0.213$, the velocity modes show strong low rank behavior and the first mode captures significantly more energy than the rest of the modes. This Strouhal number corresponds to the fundamental screech frequency observed in Fig. 9, at which the flow instability is amplified by a feedback loop as suggested by Tam [74]. Fig. 11(a) shows that the first mode at $St = 0.213$ contains approximately 2.4% of the total energy, which is comparable to the energy extracted by the first modes at lower frequencies (i.e. $St \leq 0.1$). On the other hand, we observe in Fig. 11(b) that the first mode at $St = 0.213$ captures about 45% of the energy of that Strouhal number.

Contour plots of the real part of the axial component of the leading velocity modes at $St = 0.095$, 0.213, 0.308, and 0.402 are shown in Fig. 12. The leading modes extract the most energetic structures at each frequency from the flow-field. At low frequency (Fig. 12(a)), the leading mode captures large-scale turbulent structures near the end of the potential core at $x/D \geq 7$. At $St = 0.213$ (Fig. 12(b)), which corresponds to the screech frequency, the leading mode shows strong coherence along the shear layer from the nozzle outlet to approximately $x/D = 12$. This mode takes the form of a growing and decaying instability wave, and reaches its maximum amplitude around $x/D = 5$. Figure 12(c) and 12(d) present the leading modes at the peak Strouhal numbers of the primary BBSAN lobe measured at $\phi = 130^\circ$

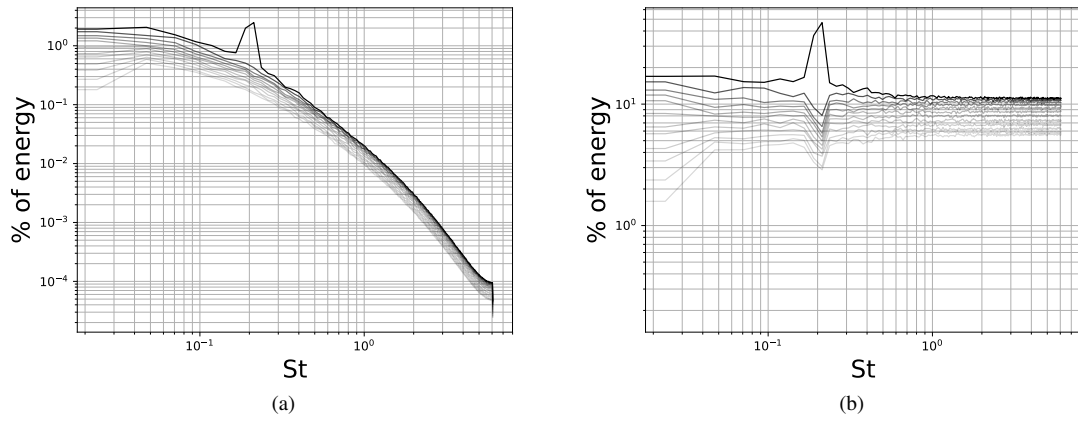


Fig. 11 Eigenvalues of POD modes of velocity vector.

and 90° . The leading modes captures finer turbulent structures along the shear layer as well as inside the jet plume, compared with lower frequencies.

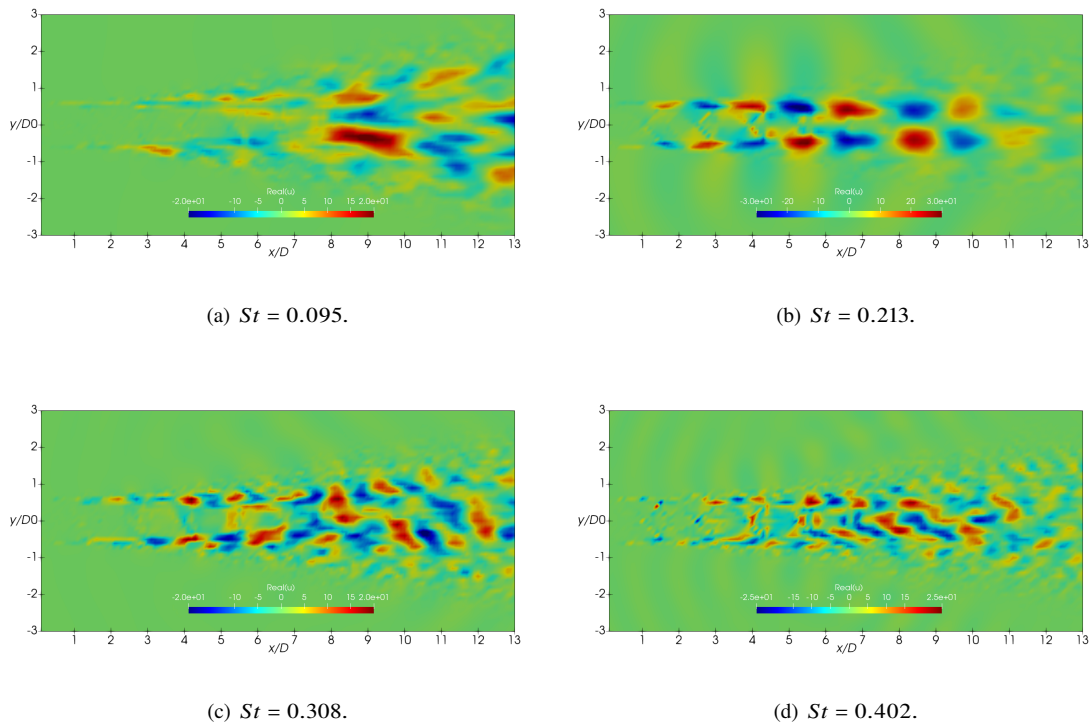


Fig. 12 Contours of the real part of the axial component of the velocity POD mode.

D. BBSAN Source Analysis

1. BBSAN Spectra

Following Section II.D, we substitute the decomposed velocity into Eq. 36 and obtain the noise source associated with BBSAN. The anisotropic velocity fluctuations can be reconstructed using different number of POD modes and their coefficients are shown in Eq. (48). The BBSAN noise spectra can be calculated using Eq. (34) and only the term for the two-point cross-correlation of BBSAN (Θ_s) is retained. Using the cross-correlation Theorem, Eq. 34 becomes

$$S(\mathbf{x}, f) = \int_{-\infty}^{\infty} \cdots \int_{-\infty}^{\infty} \hat{g}_{p,s}(\mathbf{x}, \mathbf{y}; f) \hat{g}_{p,s}^*(\mathbf{x}, \mathbf{z}; f) S_{s,s}(\mathbf{y}, \mathbf{z}; f) dz dy, \quad (51)$$

where the two-point cross-spectrum $S_{s,s}$ is calculated by multiplying the Fourier transformed BBSAN source term with its complex conjugate as

$$S_{s,s}(\mathbf{y}, \mathbf{z}; f) = \hat{\Theta}_s(\mathbf{y}, f) \hat{\Theta}_s^*(\mathbf{z}, f). \quad (52)$$

We use the source term identified by Patel and Miller [56], and use it within a wave equation. We simplify the method as

$$\frac{1}{c_\infty^2} \frac{\partial^2 p'}{\partial t^2} - \nabla^2 p' = \frac{1}{c_\infty^2} \frac{\partial}{\partial t} \Theta_s, \quad (53)$$

which takes the form of the non-homogeneous wave equation. Performing the Fourier transform with respect to time, Eq. (53) becomes the non-homogeneous Helmholtz equation

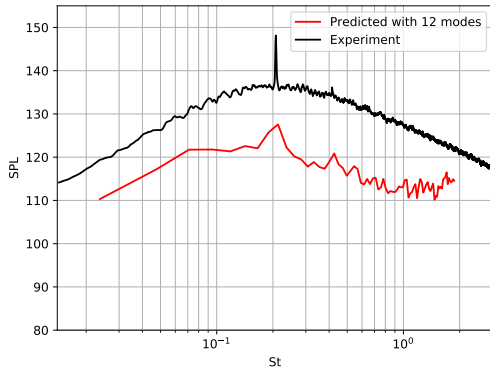
$$\frac{\omega^2}{c_\infty^2} p' + \nabla^2 p' = -\frac{i\omega}{c_\infty^2} \hat{\Theta}_s, \quad (54)$$

so that the frequency domain Green's function $\hat{g}_{p,s}$ of Eq. (51) is

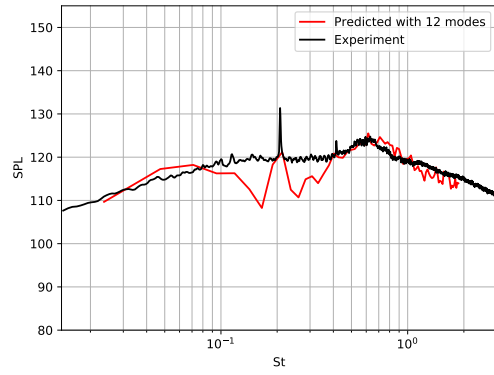
$$\hat{g}_{p,s}(\mathbf{x}, \mathbf{y}; f) = \frac{if e^{-\frac{2\pi if|\mathbf{x}-\mathbf{y}|}{c_\infty}}}{2c_\infty^2 |\mathbf{x}-\mathbf{y}|}. \quad (55)$$

Figure 13 shows the BBSAN spectra calculated with all POD modes at $\phi = 50^\circ, 80^\circ, 90^\circ,$ and 100° . The spectra is averaged over 12 flow realizations and compared with measured total noise spectra. At $\phi = 50^\circ$ (Fig. 13(a)) in the downstream direction, the BBSAN spectrum significantly under-predicts the sound pressure level (SPL) compared to the total noise spectrum. This is because in the downstream direction, BBSAN is not the dominant noise component. In the sideline and upstream directions (Fig. 14(b) to 13(d)), the shape and the amplitude of the primary BBSAN lobes are accurately captured. The peak frequencies of the primary BBSAN lobes shifts to lower frequency, which agrees with the prediction by Tam and Tanna [13]. In addition, the width of the BBSAN primary lobes also follows the trends proposed by Tam [74], where the lobe becomes narrower as the observation angle moves further upstream. These results show that the identified source term is indeed the source of BBSAN. At low frequencies, all BBSAN spectra in the sideline and upstream directions predict spurious noise. This is probably due to the same reason as the overestimation of the total spectra mentioned in Section III.B.2. The present method does not involve any empirical coefficients as the RANS approaches used by Miller [39] and Patel and Miller [56], such that errors introduced by modeling the large-scale coherent structures in the previous methods are eliminated since these data are directly obtained from the layers.

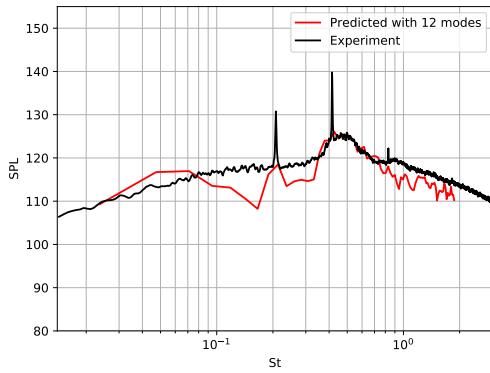
Figure 14 shows the BBSAN spectra calculated with anisotropic velocity field reconstructed using 1, 3, 7, and 12 POD modes. At $\phi = 90^\circ$ (Fig. 14(a)), the shape and amplitude of the primary BBSAN lobe is preserved when 7 POD modes are used for reconstruction. However, when only 3 modes are used, the shape of the primary lobe is no longer preserved. This indicates that the large-scale turbulent structures associated with BBSAN at $\phi = 90^\circ$ are completely captured with 7 POD modes, while higher POD modes represent fine-scale turbulent structures that are inefficient for producing BBSAN. At 100° , the primary lobe is narrower than at 90° . Only 3 POD modes are needed to capture the shape of the primary lobe in the noise spectra at this observation angle. According to Tam [74], as the width of the primary lobe gets narrower, fewer instability wave modes are involved in the generation of BBSAN. The present approach predicts this trend where less POD modes are necessary to predict BBSAN as the observation angle increases.



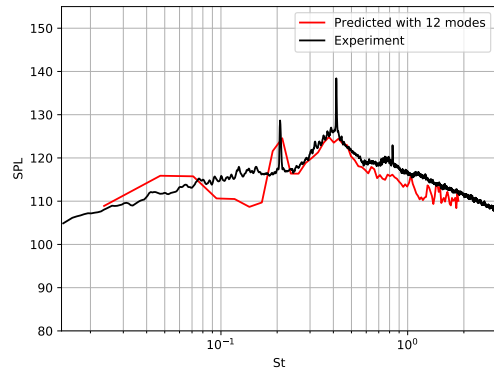
(a) $\phi = 50^\circ$.



(b) $\phi = 80^\circ$.

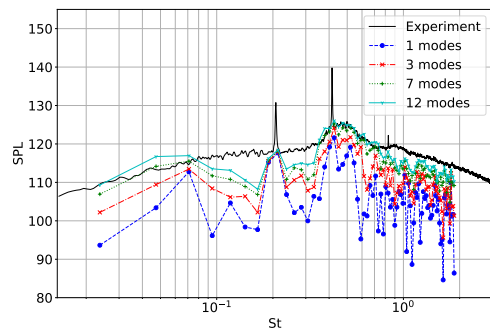


(c) $\phi = 90^\circ$.

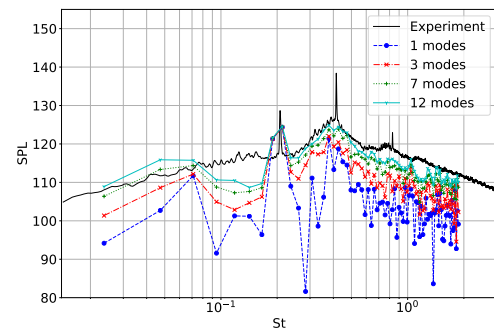


(d) $\phi = 100^\circ$.

Fig. 13 BBSAN spectra compared with measured total noise spectra.



(a) $\phi = 90^\circ$.



(b) $\phi = 100^\circ$.

Fig. 14 BBSAN spectra at $\phi = 90^\circ$ calculated with different number of POD modes.

2. Source Distribution

In this section we calculate the source intensity of BBSAN. The source intensity is calculated using the integrand in Eq. (51), which is

$$I_s(y, f) = \hat{g}_{p,s}(\mathbf{x}, \mathbf{y}; f) \hat{\Theta}_s(\mathbf{y}, f) \int \hat{g}_{p,s}^*(\mathbf{x}, \mathbf{z}; f) \hat{\Theta}_s^*(\mathbf{z}, f) d\mathbf{z}, \quad (56)$$

where \mathbf{x} is the observation location and f is the frequency. The magnitude of source intensity is calculated and averaged over 12 flow realizations. Figure 15 shows the magnitude of source intensity at $\phi = 90^\circ$ and $St = 0.497$ calculated using different number of POD modes. The selected Stouhal number corresponds to the peak BBSAN frequency at this observation angle. In Fig. 15(a), where the source intensity is calculated using 12 modes, the majority of the source intensity is observed on the oblique shocks and the region near the end of potential core. Podboy et al. [75] measured the source location of BBSAN of a similar under-expanded jet at the same observation angle using a beamforming technique. They found that BBSAN mainly comes from the end of potential core where the pressure gradient is relatively weak. Hence, the present method is capable to predict the major source locations of BBSAN, except that high values of source intensity on the oblique shock waves inside of the jet plume shown in Fig. 15 is absent in the beamforming results. This is likely due to a very low resolution of the beamforming technique of Podboy et al. [75]. Alternatively, the source intensity calculated with 7 modes shown in Fig. 15(d) demonstrates the same distribution as that calculated with 12 modes, only with slightly lower magnitude at source locations. This is aligned with the viewpoint that fine-scale turbulent structures are captured by higher POD modes. As the number of modes used for the calculation further decreases (Fig. 15(a) and 15(b)), the source distribution significantly changes and the spectra fails to capture the complete BBSAN.

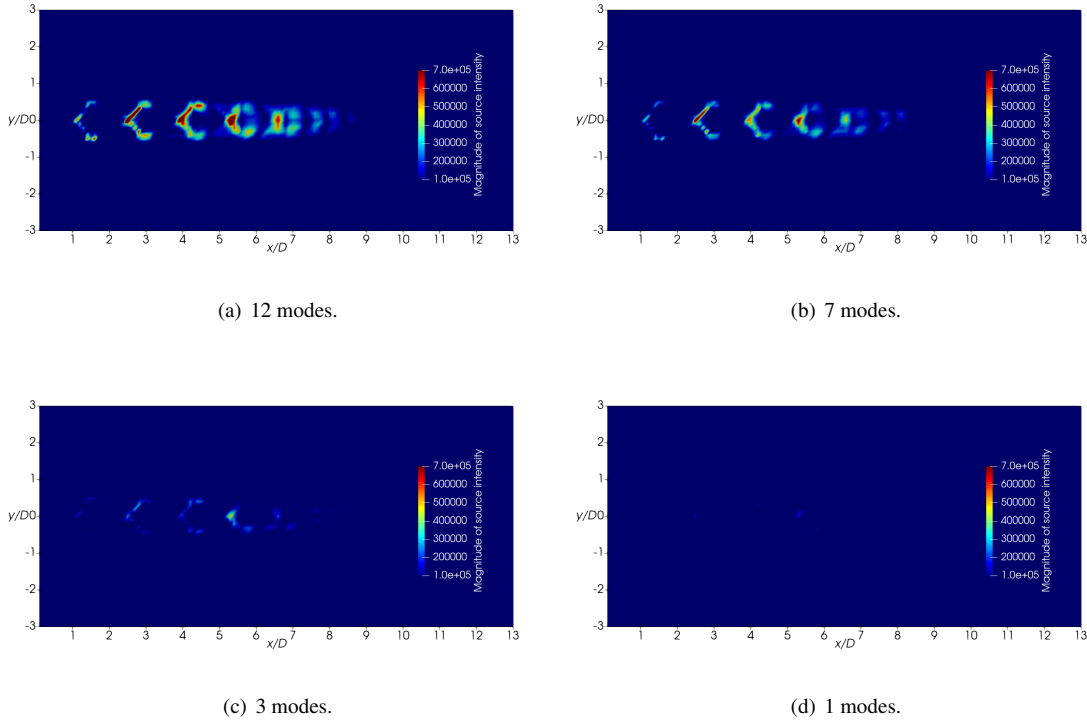


Fig. 15 Contour of BBSAN source intensity at $\phi = 90^\circ$ and $St = 0.497$ calculated with different number of POD modes.

3. Source Correlation

The two-point cross-correlation of the axial fluctuating velocity along the lip-line at $x_0/D = 3.0$ and 4.5 are plotted in Fig. 16, where the subscript 0 indicates the reference point. The selected locations correspond to the BBSAN source

locations shown in Fig. 15. The results obtained from the LES solution (Fig. 16(a) and 16(c)) are compared with those calculated using the RANS solution and the Ribner’s model [40] (Fig. 16(b) and 16(d)). Ribner’s model is

$$R(\eta, \tau) = \exp(-|\tau|/\tau_s) \exp[-(\eta - u_c \tau)^2/l^2], \quad (57)$$

where η is the separation distance in the streamwise direction, τ is the time lag, u_c is the convective velocity, τ_s is the correlation time scale, and l is the correlation length scale. The two-point cross-correlation is normalized using

$$\hat{R}(x_0, x_0 + \eta, \tau) = \frac{R(x_0, x_0 + \eta, \tau)}{\sqrt{R(x_0, x_0, 0)R(x_0 + \eta, x_0 + \eta, 0)}}, \quad (58)$$

so that its value varies between $[-1, 1]$. The correlation obtained from LES decays very slow. Therefore, we truncate the correlation value below $\exp[-1]$, so that values below this threshold are considered as random noise and filtered.

In general, both the LES and RANS results show similar correlation patterns in Fig. 16. The correlation time scales at the two locations are 6.2×10^{-5} s and 1.2×10^{-4} s in the LES results and 1.5×10^{-4} s and 2.1×10^{-4} s in the RANS results. Meanwhile, the correlation length scales are $0.26D$ and $0.36D$ in the LES results and $0.12D$ and $0.19D$ in the RANS results. The convective velocity in the LES results calculated using the slope of the correlation pattern are 435 m/s at $x_0/D = 3.0$ and 527 m/s at $x_0/D = 4.5$, respectively. On the other hand, the convective velocity in the RANS results are equal to the local time-averaged axial velocity, which are 464 m/s at $x_0/D = 3.0$ and 458 m/s at $x_0/D = 4.5$, respectively. In conclusion, the RANS results predict smaller correlation length scales and larger correlation time scales compared to the LES results. The convection velocity obtained from the LES result experiences a growth in the downstream direction, while it decays monotonically in the RANS result. The increase of the convective velocity in the downstream direction captured by the LES is also observed by Gojon et al. [76].

The two-point cross-correlation of the BBSAN source term along the lip-line at $x_0/D = 3.0$ and 4.5 are plotted in Fig. 17. The results obtained from the LES solution (Fig. 17(a) and 17(c)) are compared with those calculated using the RANS solution (Fig. 17(b) and 17(d)). The two-point cross-correlation is calculated using the inverse Fourier transformation of the cross-spectrum of the BBSAN source term as following

$$R_{s,s}(x_0, x_0 + \eta, \tau) = \int_{-\infty}^{\infty} S_{s,s}(x_0, x_0 + \eta) e^{2\pi i f \tau} df. \quad (59)$$

Again, the correlation is normalized using Eq. (58). A correlation which has an absolute value smaller than $\exp[-1]$ is truncated due to the slow decay of the correlation within LES.

Strong negative correlation paired with positive correlation can be observed in Fig. 17 due to the shock wave shear layer interaction. In the LES result, the source term is only correlated with the local shock wave at $x_0/D = 3.0$, while a correlation between the local shock wave and the neighboring shock wave in the downstream is observed at $x_0/D = 4.5$. However, the correlation with both upstream and downstream shock waves can be observed at both $x_0/D = 3.0$ and 4.5 in the RANS results. This is due to the larger correlation time scales in the RANS results compared to the LES results.

The two-point cross-correlation of the BBSAN source term along the lip-line at $x_0/D = 4.5$ calculated with only the leading POD mode is plotted in Fig. 18. Compared to the correlation calculated with the complete flow-field (Fig. 17(c)), the result calculated with only the leading POD mode shows a much stronger correlation with the neighboring shock waves in both space and time. This result shows that POD is capable to extract large-scale coherent structures that are related to the generation of BBSAN.

IV. Summary and Conclusion

In the present work, we modified a high-order compressible LES solver for supersonic jet simulation. We simulated a heated under-expanded supersonic jet from NASA’s SHJAR database. The far-field noise at different observation angles are computed using the FWH method and are compared with experimental data. Good agreements are obtained at both upstream and shallow downstream angles, where BBSAN and large-scale mixing noise are dominant, respectively. The peak frequencies of the primary BBSAN lobes at different angles are accurately captured. However, for a subset of angles where fine-scale turbulent mixing noise dominates, an 8 dB over-prediction is observed. The additional noise is probably due to poor grid resolution and the non-turbulent boundary layer at the nozzle exit.

A source term for BBSAN was identified using the decomposition of the Navier-Stokes equations. This source term consists of anisotropic velocity fluctuations multiplied by the gradient of mean pressure, where the anisotropic velocity fluctuations are obtained by decomposing the flow-field using POD and reconstructing it using different number

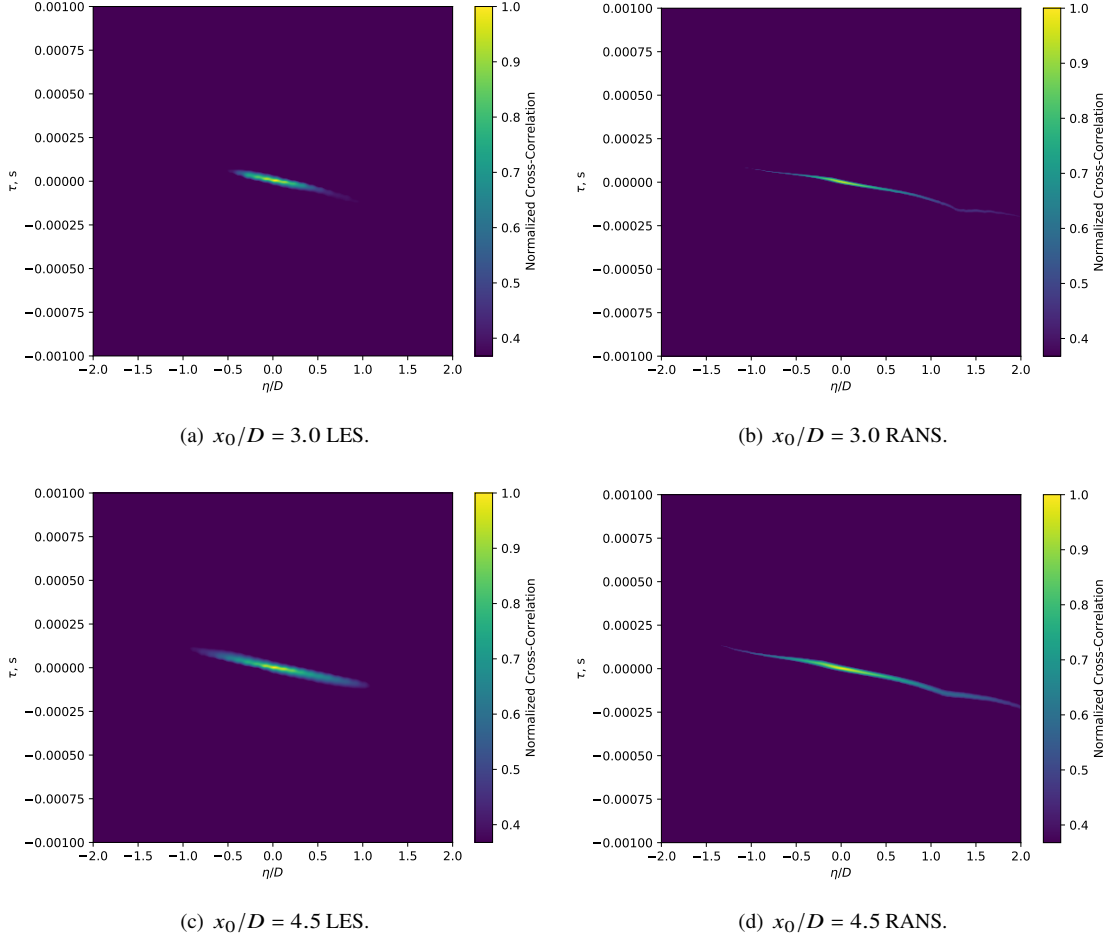


Fig. 16 Normalized two-point cross-correlation of the axial component of the fluctuating velocity along the lip-line.

of modes. The shape and amplitude of the primary BBSAN lobes are accurately predicted at sideline and upstream directions. The shape of the primary BBSAN lobe is preserved when the flow-field is reconstructed using 7 modes at $\phi = 90^\circ$ and 3 modes at $\phi = 100^\circ$. BBSAN source distribution at the peak BBSAN frequency at $\phi = 90^\circ$ shows good agreement with the experimental beamforming results by Podoy et al. [75]. The distribution is preserved when 7 modes are used for the reconstruction.

The two-point cross-correlations of the axial fluctuating velocity calculated with the LES solution are compared with the RANS results. The growth of convective velocity in the streamwise direction is only captured by the LES results. The two-point cross-correlation of the BBSAN source term shows strong positive and negative correlations at the local and neighboring shock locations. The source term correlation calculated with only the leading POD mode shows much stronger correlation between the local shock wave and the neighboring shock waves. This implies that the coherent structures extracted by POD are closely related with the generation of BBSAN.

Acknowledgements

This research was supported by the Office of Naval Research Grant N00014-17-1-2583. Any opinions, findings, and conclusions or recommendations expressed in this material are those of the author(s) and do not necessarily reflect the views of the Office of Naval Research.

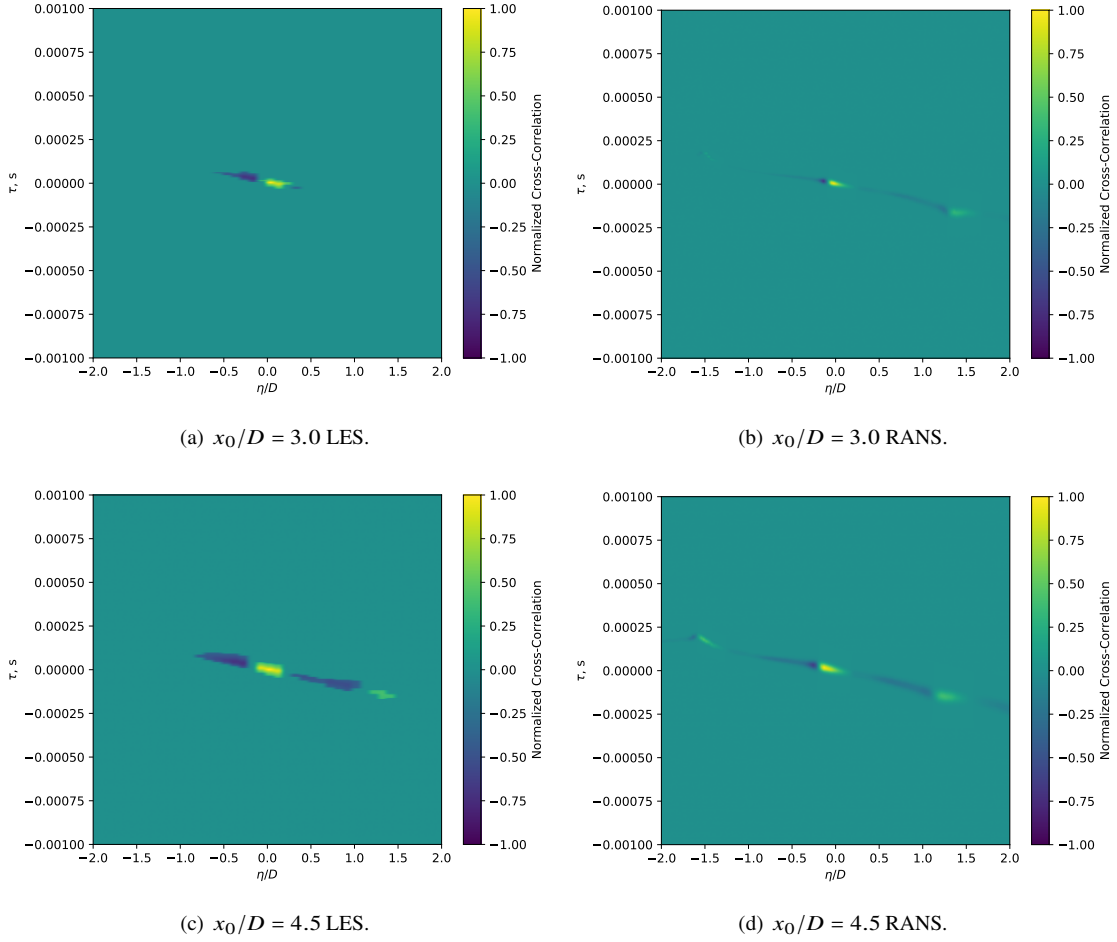


Fig. 17 Normalized two-point cross-correlation of the BBSAN source term along the lip-line.

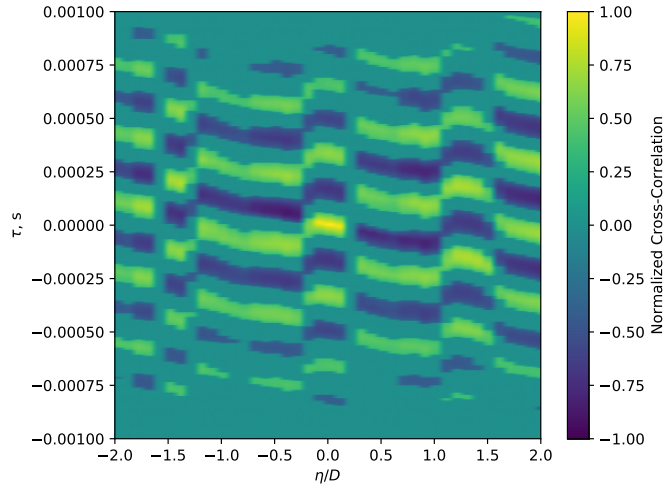


Fig. 18 Normalized two-point cross-correlation of the BBSAN source term using the leading POD mode at $x_0/D = 4.5$.

References

- [1] Doychak, J., "Department of Navy Jet Noise Reduction Project Overview," *15th Annual Partners in Environmental Technology Technical Symposium and Workshop*, Washington D.C., 2010. URL <https://apps.dtic.mil/dtic/tr/fulltext/u2/a553981.pdf>.
- [2] Williams, J. F., "Hydrodynamic Noise," *Annual Review of Fluid Mechanics*, Vol. 1, No. 1, 1969, pp. 197–222.
- [3] Brown, G. L., and Roshko, A., "On Density Effects and Large Structure in Turbulent Mixing Layers," *Journal of Fluid Mechanics*, Vol. 64, No. 4, 1974, pp. 775–816. doi:10.1017/s002211207400190x.
- [4] Townsend, A., *The Structure of Turbulent Shear Flow*, Cambridge University Press, 1980.
- [5] Mollo-Christensen, E., "Jet Noise and Shear Flow Instability Seen from an Experimenter's Viewpoint," *Journal of Applied Mechanics*, Vol. 34, No. 1, 1967, pp. 1–7. doi:10.1115/1.3607624.
- [6] Tam, C. K. W., "Supersonic Jet Noise," *Annual Review of Fluid Mechanics*, Vol. 27, No. 1, 1995, pp. 17–43. doi:10.1146/annurev.fl.27.010195.000313.
- [7] Tam, C. K. W., and Chen, K. C., "A Statistical Model of Turbulence in Two-Dimensional Mixing Layers," *Journal of Fluid Mechanics*, Vol. 92, No. 2, 1979, pp. 303–326. doi:10.1017/s002211207900063x.
- [8] Tam, C. K. W., and Morris, P. J., "The Radiation of Sound by the Instability Waves of a Compressible Plane Turbulent Shear Layer," *Journal of Fluid Mechanics*, Vol. 98, No. 2, 1980, pp. 349–381. doi:10.1017/s0022112080000195.
- [9] Tam, C. K. W., and Burton, D. E., "Sound Generated by Instability Waves of Supersonic Flows. Part 1. Two-Dimensional Mixing Layers," *Journal of Fluid Mechanics*, Vol. 138, No. -1, 1984, p. 249. doi:10.1017/s0022112084000112.
- [10] Tam, C. K. W., and Burton, D. E., "Sound Generated by Instability Waves of Supersonic Flows. Part 2. Axisymmetric Jets," *Journal of Fluid Mechanics*, Vol. 138, No. -1, 1984, p. 273. doi:10.1017/s0022112084000124.
- [11] Jordan, P., and Colonius, T., "Wave Packets and Turbulent Jet Noise," *Annual Review of Fluid Mechanics*, Vol. 45, No. 1, 2013, pp. 173–195. doi:10.1146/annurev-fluid-011212-140756.
- [12] Harper-Bourne, M., and Fisher, M. J., "The Noise from Shock Waves in Supersonic Jets," AGARD conference proceedings No. 131, 1973, pp. 11–1.
- [13] Tam, C. K. W., and Tanna, H. K., "Shock Associated Noise of Supersonic Jets from Convergent-Divergent Nozzles," *Journal of Sound and Vibration*, Vol. 81, No. 3, 1982, pp. 337–358. doi:10.1016/0022-460x(82)90244-9.
- [14] Tam, C. K. W., "Stochastic Model Theory of Broadband Shock Associated Noise from Supersonic Jets," *Journal of Sound and Vibration*, Vol. 116, No. 2, 1987, pp. 265–302. doi:10.1016/s0022-460x(87)81303-2.
- [15] Morris, P. J., and Miller, S. A. E., "Prediction of Broadband Shock-Associated Noise Using Reynolds-Averaged Navier-Stokes Computational Fluid Dynamics," *AIAA Journal*, Vol. 48, No. 12, 2010, pp. 2931–2944. doi:10.2514/1.j055060.
- [16] Suzuki, T., "Wave-Packet Representation of Shock-Cell Noise for a Single Round Jet," *AIAA Journal*, Vol. 54, No. 12, 2016, pp. 3903–3917. doi:10.2514/1.j055097.
- [17] Choi, H., and Moin, P., "Grid-Point Requirements for Large Eddy Simulation: Chapman's Estimates Revisited," *Physics of Fluids*, Vol. 24, No. 1, 2012, p. 011702. doi:10.1063/1.3676783.
- [18] Williams, J. E. F., and Hawkings, D. L., "Sound Generation by Turbulence and Surfaces in Arbitrary Motion," *Philosophical Transactions of the Royal Society A: Mathematical, Physical and Engineering Sciences*, Vol. 264, No. 1151, 1969, pp. 321–342. doi:10.1098/rsta.1969.0031.
- [19] Boersma, B., and Lele, S., "Large Eddy Simulation of a Mach 0.9 Turbulent Jet," *5th AIAA/CEAS Aeroacoustics Conference and Exhibit*, American Institute of Aeronautics and Astronautics (AIAA), 1999. doi:10.2514/6.1999-1874.
- [20] Bodony, D. J., and Lele, S. K., "On Using Large-Eddy Simulation for the Prediction of Noise from Cold and Heated Turbulent Jets," *Physics of Fluids*, Vol. 17, No. 8, 2005, p. 085103. doi:10.1063/1.2001689.
- [21] Shur, M., Spalart, P., Strelets, M., and Garbaruk, A., "Further Steps in LES-Based Noise Prediction for Complex Jets," *44th AIAA Aerospace Sciences Meeting and Exhibit*, American Institute of Aeronautics and Astronautics (AIAA), 2006. doi:10.2514/6.2006-485.

- [22] Brès, G. A., Ham, F. E., Nichols, J. W., and Lele, S. K., “Unstructured Large-Eddy Simulations of Supersonic Jets,” *AIAA Journal*, Vol. 55, No. 4, 2017, pp. 1164–1184. doi:10.2514/1.j055084.
- [23] Mendez, S., Shoeybi, M., Sharma, A., Ham, F. E., Lele, S. K., and Moin, P., “Large-Eddy Simulations of Perfectly Expanded Supersonic Jets Using an Unstructured Solver,” *AIAA Journal*, Vol. 50, No. 5, 2012, pp. 1103–1118. doi:10.2514/1.j051211.
- [24] Liu, J., Corrigan, A. T., Kailasanath, K., Heeb, N. S., Munday, D. E., and Gutmark, E. J., “Computational Study of Shock-Associated Noise Characteristics Using LES,” *19th AIAA/CEAS Aeroacoustics Conference*, American Institute of Aeronautics and Astronautics (AIAA), 2013. doi:10.2514/6.2013-2199.
- [25] Brès, G. A., Jaunet, V., Rallic, M. L., Jordan, P., Colonius, T., and Lele, S. K., “Large Eddy Simulation for Jet Noise: The Importance of Getting the Boundary Layer Right,” *21st AIAA/CEAS Aeroacoustics Conference*, American Institute of Aeronautics and Astronautics (AIAA), 2015. doi:10.2514/6.2015-2535.
- [26] Liu, J., and Corrigan, A. T., “Large-Eddy Simulations of Supersonic Jet Noise Generation Using Wall Modeling,” *2018 AIAA/CEAS Aeroacoustics Conference*, American Institute of Aeronautics and Astronautics (AIAA), 2018. doi:10.2514/6.2018-3943.
- [27] Liu, J., and Ramamurti, R., “Numerical Study of Supersonic Jet Noise Emanating from an F404 Nozzle at Model Scale,” *AIAA Scitech 2019 Forum*, American Institute of Aeronautics and Astronautics (AIAA), 2019. doi:10.2514/6.2019-0807.
- [28] Hesthaven, J. S., and Warburton, T., *Nodal Discontinuous Galerkin Methods*, Springer New York, 2008. doi:10.1007/978-0-387-72067-8.
- [29] May, G., and Jameson, A., “A Spectral Difference Method for the Euler and Navier-Stokes Equations on Unstructured Meshes,” *44th AIAA Aerospace Sciences Meeting and Exhibit*, American Institute of Aeronautics and Astronautics (AIAA), 2006. doi:10.2514/6.2006-304.
- [30] Corrigan, A. T., Kercher, A., Liu, J., and Kailasanath, K., “Jet Noise Simulation using a Higher-Order Discontinuous Galerkin Method,” *2018 AIAA Aerospace Sciences Meeting*, American Institute of Aeronautics and Astronautics (AIAA), 2018. doi:10.2514/6.2018-1247.
- [31] Spiegel, S. C., DeBonis, J. R., and Huynh, H., “Overview of the NASA Glenn Flux Reconstruction Based High-Order Unstructured Grid Code,” *54th AIAA Aerospace Sciences Meeting*, AIAA, 2016. doi:10.2514/6.2016-1061.
- [32] Lumley, J. L., “The Structure of Inhomogeneous Turbulence,” *Atmospheric Turbulence and Wave Propagation*, 1967, pp. 166–178.
- [33] Taira, K., Brunton, S. L., Dawson, S. T. M., Rowley, C. W., Colonius, T., McKeon, B. J., Schmidt, O. T., Gordeyev, S., Theofilis, V., and Ukeiley, L. S., “Modal Analysis of Fluid Flows: An Overview,” *AIAA Journal*, Vol. 55, No. 12, 2017, pp. 4013–4041. doi:10.2514/1.j056060.
- [34] Arndt, R. E. A., Long, D. F., and Glauser, M. N., “The Proper Orthogonal Decomposition of Pressure Fluctuations Surrounding a Turbulent Jet,” *Journal of Fluid Mechanics*, Vol. 340, 1997, pp. 1–33. doi:10.1017/s0022112097005089.
- [35] Schmidt, O. T., Towne, A., Rigas, G., Colonius, T., and Brès, G. A., “Spectral Analysis of Jet Turbulence,” *Journal of Fluid Mechanics*, Vol. 855, 2018, pp. 953–982. doi:10.1017/jfm.2018.675.
- [36] Gordeyev, S. V., and Thomas, F. O., “Coherent Structure in the Turbulent Planar Jet. Part 1. Extraction of Proper Orthogonal Decomposition Eigenmodes and Their Self-Similarity,” *Journal of Fluid Mechanics*, Vol. 414, 2000, pp. 145–194. doi:10.1017/s002211200000848x.
- [37] Freund, J. B., and Colonius, T., “Turbulence and Sound-Field POD Analysis of a Turbulent Jet,” *International Journal of Aeroacoustics*, Vol. 8, No. 4, 2009, pp. 337–354. doi:10.1260/147547209787548903.
- [38] Brown, C., and Bridges, J., “Small Hot Jet Acoustic Rig Validation,” 2006. NASA/TM-2006-214234.
- [39] Miller, S. A. E., “Noise from Isotropic Turbulence,” *AIAA Journal*, Vol. 55, No. 3, 2017, pp. 755–773. doi:10.2514/1.j055114.
- [40] Ribner, H., “Two point correlations of jet noise,” *Journal of Sound and Vibration*, Vol. 56, No. 1, 1978, pp. 1–19. doi:10.1016/0022-460x(78)90566-7.
- [41] Wagner, C., Hüttl, T., and Sagaut, P. (eds.), *Large-Eddy Simulation for Acoustics*, Cambridge University Press, 2007. doi:10.1017/cbo9780511546143.

- [42] Nicoud, F., and Ducros, F., “Subgrid-Scale Stress Modelling Based on the Square of the Velocity Gradient Tensor,” *Flow, turbulence and Combustion*, Vol. 62, No. 3, 1999, pp. 183–200. doi:10.1023/a:1009995426001.
- [43] López, M. R., Sheshadri, A., Bull, J. R., Economou, T. D., Romero, J., Watkins, J. E., Williams, D. M., Palacios, F., Jameson, A., and Manosalvas, D. E., “Verification and Validation of HiFiLES: a High-Order LES unstructured solver on multi-GPU platforms,” *32nd AIAA Applied Aerodynamics Conference*, AIAA Paper No. 2014-3168, 2014. doi:10.2514/6.2014-3168.
- [44] Vincent, P. E., Castonguay, P., and Jameson, A., “A New Class of High-Order Energy Stable Flux Reconstruction Schemes,” *Journal of Scientific Computing*, Vol. 47, No. 1, 2010, pp. 50–72. doi:10.1007/s10915-010-9420-z.
- [45] Toro, E. F., *Riemann Solvers and Numerical Methods for Fluid Dynamics: A Practical Introduction*, Springer Science & Business Media, 2013.
- [46] Huynh, H. T., “A Reconstruction Approach to High-Order Schemes Including Discontinuous Galerkin for Diffusion,” *47th AIAA Aerospace Sciences Meeting including The New Horizons Forum and Aerospace Exposition*, AIAA Paper No. 2009-403, 2009. doi:10.2514/6.2009-403.
- [47] Huynh, H. T., “A Flux Reconstruction Approach to High-Order Schemes Including Discontinuous Galerkin Methods,” *18th AIAA Computational Fluid Dynamics Conference*, American Institute of Aeronautics and Astronautics, 2007. doi:10.2514/6.2007-4079, URL <https://doi.org/10.2514/6.2007-4079>.
- [48] Castonguay, P., Williams, D., Vincent, P., and Jameson, A., “Energy Stable Flux Reconstruction Schemes for Advection–Diffusion Problems,” *Computer Methods in Applied Mechanics and Engineering*, Vol. 267, 2013, pp. 400 – 417. doi:<https://doi.org/10.1016/j.cma.2013.08.012>.
- [49] Hesthaven, J. S., and Kirby, R. M., “Filtering in Legendre Spectral Methods,” *Mathematics of Computation*, Vol. 77, No. 263, 2008, pp. 1425–1452. doi:10.1090/s0025-5718-08-02110-8.
- [50] Persson, P.-O., “Shock Capturing for High-Order Discontinuous Galerkin Simulation of Transient Flow Problems,” *21st AIAA Computational Fluid Dynamics Conference*, AIAA Paper No. 2013-3061, 2013. doi:10.2514/6.2013-3061.
- [51] Park, J. S., and Kim, C., “Hierarchical Multi-Dimensional Limiting Strategy for Correction Procedure via Reconstruction,” *Journal of Computational Physics*, Vol. 308, 2016, pp. 57–80. doi:10.1016/j.jcp.2015.12.020.
- [52] Lighthill, M. J., “On Sound Generated Aerodynamically I. General Theory,” *Proceedings of the Royal Society of London. Series A. Mathematical and Physical Sciences*, Vol. 211, No. 1107, 1952, pp. 564–587. doi:10.1098/rspa.1952.0060.
- [53] Lighthill, M. J., “On Sound Generated Aerodynamically II. Turbulence as a Source of Sound,” *Proceedings of the Royal Society of London. Series A. Mathematical and Physical Sciences*, Vol. 222, No. 1148, 1954, pp. 1–32. doi:10.1098/rspa.1954.0049.
- [54] Spalart, P. R., and Shur, M. L., “Variants of the Ffowcs Williams - Hawkins Equation and Their Coupling with Simulations of Hot Jets,” *International Journal of Aeroacoustics*, Vol. 8, No. 5, 2009, pp. 477–491. doi:10.1260/147547209788549280.
- [55] Farassat, F., “Derivation of Formulations 1 and 1A of Farassat,” 2007. NASA/TM-2007-214853.
- [56] Patel, T. K., and Miller, S. A. E., “Statistical Sources for Broadband Shock-Associated Noise Using the Navier-Stokes Equations,” 2020. Manuscript submitted for publication.
- [57] Tam, C. K. W., and Auriault, L., “Jet Mixing Noise from Fine-Scale Turbulence,” *AIAA Journal*, Vol. 37, No. 2, 1999, pp. 145–153. doi:10.2514/2.691.
- [58] Towne, A., Schmidt, O. T., and Colonius, T., “Spectral Proper Orthogonal Decomposition and Its Relationship to Dynamic Mode Decomposition and Resolvent Analysis,” *Journal of Fluid Mechanics*, Vol. 847, 2018, pp. 821–867. doi:10.1017/jfm.2018.283.
- [59] Welch, P., “The Use of Fast Fourier Transform for the Estimation of Power Spectra: A Method Based on Time Averaging over Short, Modified Periodograms,” *IEEE Transactions on Audio and Electroacoustics*, Vol. 15, No. 2, 1967, pp. 70–73. doi:10.1109/tau.1967.1161901.
- [60] Brès, G., Nichols, J., Lele, S., and Ham, F., “Towards Best Practices for Jet Noise Predictions with Unstructured Large Eddy Simulations,” 2012. doi:10.2514/6.2012-2965.
- [61] Mendez, S., Shoeybi, M., Lele, S. K., and Moin, P., “On the Use of the Ffowcs Williams–Hawkins Equation to Predict Far-Field Jet Noise from Large-Eddy Simulations,” *International Journal of Aeroacoustics*, Vol. 12, No. 1-2, 2013, pp. 1–20. doi:10.1260/1475-472x.12.1-2.1.

- [62] Shur, M. L., Spalart, P. R., and Strelets, M. K., “Noise Prediction for Increasingly Complex Jets. Part I: Methods and Tests,” *International Journal of Aeroacoustics*, Vol. 4, No. 3, 2005, pp. 213–245. doi:10.1260/1475472054771376.
- [63] Liu, J., Kailasanath, K., Heeb, N., Munday, D., and Gutmark, E., “Large-Eddy Simulations of a Supersonic Heated Jet,” *17th AIAA/CEAS Aeroacoustics Conference (32nd AIAA Aeroacoustics Conference)*, AIAA Paper No. 2011-2884, 2011. doi:10.2514/6.2011-2884.
- [64] Tam, C. K. W., “Mach Wave Radiation from High-Speed Jets,” *AIAA Journal*, Vol. 47, No. 10, 2009, pp. 2440–2448. doi:10.2514/1.42644.
- [65] “ANSYS® Fluent Academic Research Mechanical, Release 18.1,” , 2019.
- [66] Menter, F., “Zonal Two Equation k-w Turbulence Models For Aerodynamic Flows,” *23rd Fluid Dynamics, Plasmadynamics, and Lasers Conference*, AIAA, 1993. doi:10.2514/6.1993-2906.
- [67] SARKAR, S., and LAKSHMANAN, B., “Application of a Reynolds Stress Turbulence Model to the Compressible Shear Layer,” *AIAA Journal*, Vol. 29, No. 5, 1991, pp. 743–749. doi:10.2514/3.10649.
- [68] Menter, F. R., “Two-Equation Eddy-Viscosity Turbulence Models for Engineering Applications,” *AIAA Journal*, Vol. 32, No. 8, 1994, pp. 1598–1605. doi:10.2514/3.12149.
- [69] Georgiadis, N. J., Yoder, D. A., and Engblom, W. B., “Evaluation of Modified Two-Equation Turbulence Models for Jet Flow Predictions,” *AIAA Journal*, Vol. 44, No. 12, 2006, pp. 3107–3114. doi:10.2514/1.22650.
- [70] Lele, S. K., Mendez, S., Ryu, J., Nichols, J., Shoeybi, M., and Moin, P., “REprint of: Sources of High-Speed Jet Noise: Analysis of LES Data and Modeling,” *Procedia IUTAM*, Vol. 1, 2010, pp. 84–93. doi:10.1016/j.piutam.2010.10.010.
- [71] Liu, J., Corrigan, A. T., Kailasanath, K., Heeb, N. S., and Gutmark, E. J., “Numerical Study of Noise Sources Characteristics in An Underexpanded Jet Flow,” *20th AIAA/CEAS Aeroacoustics Conference*, American Institute of Aeronautics and Astronautics (AIAA), 2014. doi:10.2514/6.2014-2604.
- [72] Bridges, J., and Brown, C., “Validation of the Small Hot Jet Acoustic Rig for Aeroacoustic Research,” *11th AIAA/CEAS Aeroacoustics Conference*, AIAA Paper No. 2005-2846, 2005. doi:10.2514/6.2005-2846.
- [73] Bogey, C., and Bailly, C., “Influence of Nozzle-Exit Boundary-Layer Conditions on the Flow and Acoustic Fields of Initially Laminar Jets,” *Journal of Fluid Mechanics*, Vol. 663, 2010, pp. 507–538. doi:10.1017/s0022112010003605.
- [74] Tam, C. K. W., Seiner, J., and Yu, J., “Proposed Relationship between Broadband Shock Associated Noise and Screech Tones,” *Journal of Sound and Vibration*, Vol. 110, No. 2, 1986, pp. 309–321. doi:10.1016/s0022-460x(86)80212-7.
- [75] Podboy, G. G., Wernet, M. P., Clem, M. M., and Fagan, A. F., “Noise Source Location and Flow Field Measurements on Supersonic Jets and Implications Regarding Broadband Shock Noise,” 2017. NASA/TM-2017-219544.
- [76] Gojon, R., Baier, F., Gutmark, E. J., and Mihaescu, M., “Temperature effects on the aerodynamic and acoustic fields of a rectangular supersonic jet,” *55th AIAA Aerospace Sciences Meeting*, American Institute of Aeronautics and Astronautics, 2017. doi:10.2514/6.2017-0002, URL <https://doi.org/10.2514/6.2017-0002>.